

Ice-proximal sea-ice reconstruction in Powell Basin, Antarctica since the Last Interglacial

Wee Wei Khoo^{1*}, Juliane Müller^{1,2,3}, Oliver Esper¹, Wenshen Xiao⁴, Christian Stepanek¹, Paul Gierz¹, Gerrit Lohmann^{1,3,5}, Walter Geibert¹, Jens Hefter¹ and Gesine Mollenhauer^{1,2,3}

¹Alfred Wegener Institute, Helmholtz Centre for Polar and Marine Research, Bremerhaven, Germany

²Department of Geoscience, University of Bremen, Bremen, Germany

³MARUM - Center for Marine Environmental Sciences, University of Bremen, Bremen, Germany

⁴State Key Laboratory of Marine Geology, Tongji University, Shanghai, China

⁵Department of Environmental Physics, University of Bremen, Bremen, Germany

Correspondence: Wee Wei Khoo (wee.wei.khoo@awi.de)

ABSTRACT. In Antarctica, the presence of sea ice not only plays a critical role in the climate system but also contributes to enhancing the stability of the floating ice shelves. Hence, investigating past ice-proximal sea-ice conditions, especially across glacial-interglacial cycles, can provide crucial information pertaining to sea-ice variability and deepen our understanding of ocean-ice-atmosphere dynamics and feedback. In this study, we apply a multiproxy approach, in combination with numerical climate modeling, to explore glacial-interglacial environmental variability. We analyze the novel sea ice biomarker IPSO₂₅ (a di-unsaturated highly branched isoprenoid (HBI)), open-water biomarkers (tri-unsaturated HBIs; z-/e-trienes), and the diatom assemblage and primary productivity indicators in a marine sediment core retrieved from Powell Basin, NW Weddell Sea. These biomarkers have been established as reliable proxies for reconstructing near-coastal sea-ice conditions in the Southern Ocean, where the typical use of sea ice-related diatoms can be impacted by silica dissolution. We present the first continuous sea-ice records, in close proximity to the Antarctic continental margin, since the penultimate deglaciation. Our data shed new light on the (seasonal) variability of sea ice in the basin, and reveal a highly dynamic glacial-interglacial sea-ice setting characterized by significant shifts from perennial ice cover to seasonal sea-ice cover and open marine environment over the last 145 kyrs. Our results also unveil a stronger deglacial amplitude and warming during the Last Interglacial (MIS 5e) compared to the current one (Holocene). A short-term sea ice readvancement also occurred towards the end of each deglaciation. Finally, despite similar findings between the proxy and model data, notable differences persist between both interglacials – emphasizing the necessity for different Antarctic ice-sheet configurations to be employed and more robust paleoclimate data to enhance climate model performance close to the Antarctic continental margin.

33 1 Introduction

34 Sea ice plays a vital role within Earth's climate system, exerting significant influence on air-sea
35 interactions, ocean circulation and ecosystem dynamics. Its presence alters the surface albedo of the
36 ocean through the reflectance of incoming solar radiation, thereby minimizing ocean warming (Ebert et
37 al., 1995). Likewise, sea ice affects the atmosphere-ocean interaction by inhibiting the exchange of
38 heat, gas and water vapor between both media (Dieckmann and Hellmer, 2010). During sea-ice
39 formation, brine rejection occurs and leads to the production of high-saline shelf water. This dense high-
40 saline shelf water then sinks towards the deeper ocean. Consequently, this process results in
41 redistribution of salinity within the water column and has a profound impact on the stratification and
42 ventilation of the ocean (Vaughan et al., 2013). For example, in a few locations in the Southern Ocean
43 (SO), such as the Weddell Sea, the high-saline shelf water – depending on its route and mixing process
44 – becomes the precursor of Antarctic Bottom Water (AABW), which is a major driver of the global
45 thermohaline circulation and an important water mass that ventilates the deep ocean basins (Naveira
46 Garabato et al., 2002; Rintoul, 2018; Seabrooke et al., 1971). Furthermore, when sea ice melts, the
47 freshened surface water mixes with the upwelled deep water, contributing to the mode and intermediate
48 waters in the Atlantic, Indian and Pacific sectors of the SO (Abernathy et al., 2016; Pellichero et al.,
49 2018). Sea ice also serves as a crucial buttressing force at the ice front, effectively preventing or
50 delaying the occurrence of potential calving events (Robel, 2017). This phenomenon was evident at
51 locations such as the Mertz Glacier Tongue (Massom et al., 2015) and the Totten Ice Shelf (Greene et
52 al., 2018) in East Antarctica. Furthermore, the presence of a sea-ice buffer in front of the ice terminus
53 acts to diminish ocean swells as they propagate towards land. For instance, Massom et al. (2018)
54 observed a substantial increase (orders of magnitude) in wave energy experienced at the fronts of the
55 Larsen ice shelves and the Wilkins Ice Shelf when the sea-ice buffer was removed. In this regard, any
56 changes to the sea-ice cover can potentially alter ice-ocean-atmosphere dynamics and ocean
57 circulation patterns, making analyses of sea-ice variability over glacial-interglacial cycles, covering
58 periods of less and more pronounced sea-ice cover, crucial.

59 Presently, numerous methods are used to reconstruct past sea-ice conditions, including biogenic
60 proxies (e.g., biomarkers, diatoms, dinoflagellate cysts, foraminifera and ostracods) and
61 sedimentological proxies (e.g., ice-rafted debris) in marine sediments, as well as chemical compounds
62 archived in ice cores (e.g., methanesulfonic acid and sea-salt (ssNa⁺); de Vernal et al., 2013 and
63 references therein). Determination of methanesulfonic acid or ssNa⁺ concentrations in Antarctic ice
64 cores permits well-dated and temporally high-resolution regional sea-ice reconstructions but is often
65 affected by other sea ice independent factors such as atmospheric transport (Abram et al., 2013). In
66 particular, direct proxies, originating from sea-ice dwelling microorganisms, which are preserved in
67 marine sediments are often preferred as they increase the reliability of sea-ice estimation (Leventer,
68 1998). Despite this, our understanding of past sea ice changes in the SO remains limited. The Cycles
69 of Sea-Ice Dynamics in the Earth System working group (C-SIDE; Chadwick et al., 2019; Rhodes et al.,
70 2019) consolidated a list of published Antarctic marine sea-ice records, as outlined in the review paper
71 by Crosta et al. (2022). The compilation documents 20 studies on sea-ice variability during the Holocene
72 (0-12 ka before present (BP)), 150 records detailing changes at the Last Glacial Maximum (LGM; ca.

73 21 ka BP or Marine Isotope Stage (MIS) 2), and a mere 14 sea-ice records dating back to around 130
74 ka BP. Notably, just two records extend beyond MIS 6 (ca. 191 ka BP; see also Fig. 3 in Crosta et al.,
75 2022). Their work underscores the pronounced dearth of (paleo) sea-ice reconstructions, particularly in
76 regions south of 60°S, notably in the Atlantic sector, and during the Last Interglacial (LIG) and beyond.
77 This scarcity of records, in particular proximal to the continental margin, is attributable to difficulties in
78 recovering marine sediment cores in the polar regions that at present are still subject to heavy year-
79 round ice cover, and a lack of continuous sedimentary records due to erosion and disturbance at the
80 sea floor during past glaciations. Moreover, limited preservation potential of silica frustules in SO
81 regions outside of the opal belt further hampers sea-ice reconstructions using diatom assemblages
82 (Ryves et al., 2009; Vernet et al., 2019). As such, important feedback mechanisms related to the sea
83 ice-ice shelf system during warmer-than-present periods and throughout climate transitions, remain
84 poorly understood. Ultimately, this lack of knowledge on how Antarctic ice sheets/shelves respond(ed)
85 to oceanic forcing may disadvantage climate models' ability to faithfully reproduce dynamics in the
86 ocean-sea ice-ice system, and limit our confidence in future projections of the Antarctic Ice Sheet's
87 contribution towards global sea level rise (Deconto and Pollard, 2016; Naughten et al., 2018). Despite
88 similar LIG-WSI retreats in marine records, inconsistency with regard to the position of the sea-ice edge,
89 in particular in the Atlantic sector, remains evident when the proposed spatial structure of the $\delta^{18}\text{O}$ -
90 agreed WSI extent is compared to published marine records (Holloway et al., 2017). Holloway et al.
91 (2017) and Crosta et al. (2022) opined that this discrepancy may result from the marine records (Bianchi
92 and Gersonde, 2002; Chadwick et al., 2020; 2022) being located too far north to adequately validate
93 the $\delta^{18}\text{O}$ -agreed WSI extent. Thus, they emphasized the need for additional marine records closer to
94 the continental margin to adequately constrain the spatial pattern of the LIG sea-ice extent.

95 In recent years, the use of a novel sea-ice biomarker has been found increasingly applicable as a
96 suitable proxy for Antarctic sea-ice reconstructions (Belt et al., 2016; Smik et al., 2016). This sea-ice
97 biomarker, a di-unsaturated C_{25} highly branched isoprenoid (HBI) alkene, introduced as an Antarctic
98 sea-ice proxy by Massé et al. (2011), was later termed Ice Proxy for the Southern Ocean with 25 carbon
99 atoms (IPSO₂₅), drawing parallel to the Arctic IP₂₅ (Belt et al., 2016). IPSO₂₅ is a lipid molecule produced
100 by the sympagic diatom *Berkeleya adeliensis*, which lives in the sea-ice matrix and is generally
101 abundant during late spring and early summer (Belt et al., 2016; Riaux-Gobin and Poulin, 2004), hence,
102 making the biomarker a good indicator for spring/summer sea ice. Furthermore, the biomarker is well-
103 preserved in the sediment and widely identified in areas near to the Antarctic continent (for more details,
104 see Belt, 2018; Belt et al., 2016). Nevertheless, there remains a risk of under-/overestimating the
105 presence of sea ice when relying solely on the IPSO₂₅ proxy. Thus, Vorrath et al. (2019) proposed
106 combining open-water phytoplankton markers like dinosterol or a HBI-triene with the IPSO₂₅ proxy, to
107 calculate the phytoplankton-IPSO₂₅ index (PIPSO₂₅). This enhances the quantitative application of the
108 IPSO₂₅ proxy. For example, in cases where the IPSO₂₅ concentration is minimal or absent, this may
109 imply either an open ocean condition (substantiated by a high phytoplankton signal) or the presence of
110 a perennial ice cover (evident by a low/absent phytoplankton signal). As such, the use of the PIPSO₂₅
111 proxy proves to be a more reliable approach to distinguish contrasting sea-ice settings (Belt and Müller,
112 2013; Lamping et al., 2020). To substantiate this application, Lamping et al. (2021) compared PIPSO₂₅-

113 derived sea-ice estimates close to the Antarctic continental margin against satellite sea-ice
114 observations and modeled sea-ice patterns, revealing strong correlation between the proxy, satellite
115 and modeled data. Until now, the majority of HBI-based sea-ice reconstructions has focused on
116 Holocene and deglacial/LGM time scales (e.g., Barbara et al., 2013; 2016; Denis et al., 2010; Etourneau
117 et al., 2013; Lamping et al., 2020; Sadatzki et al., 2023; Vorrath et al., 2020, 2023) and one
118 reconstruction dates back to the last ca. 60 ka BP (Collins et al., 2013). Yet, this tool has not been
119 applied towards studying sea-ice variability in the Antarctic during warm climates beyond the current
120 interglacial.

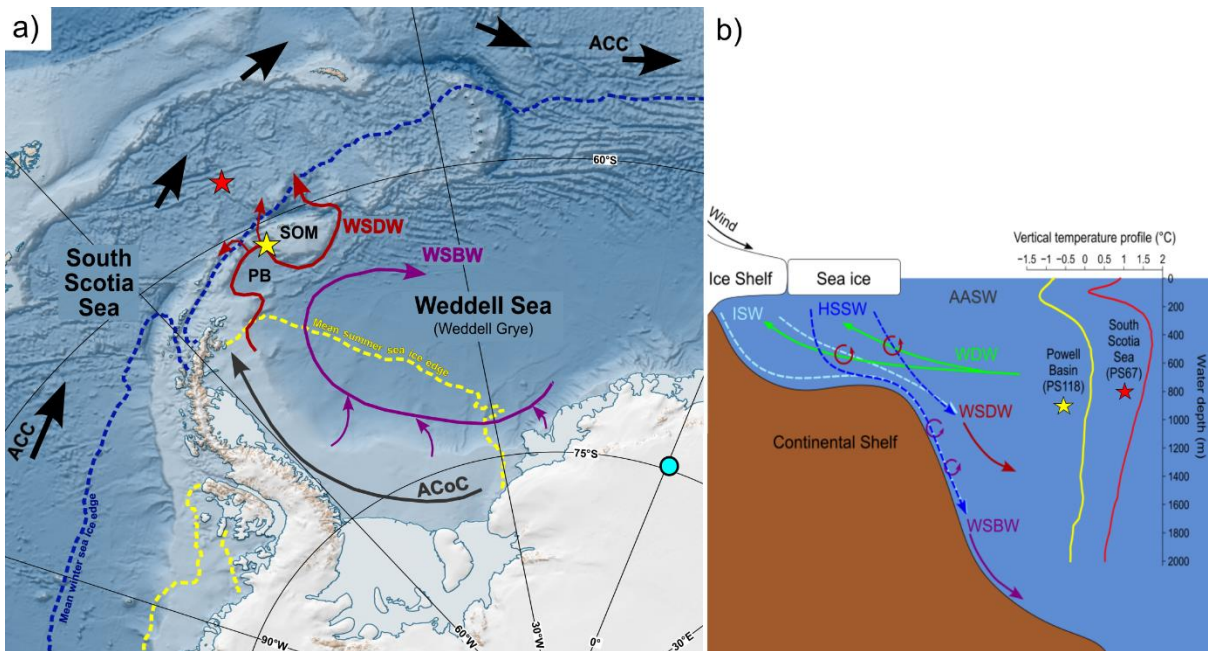
121 Here, we aim to investigate the glacial-interglacial environmental variability in the Powell Basin,
122 NW Weddell Sea through a multiproxy approach, and provide the first continuous ice-proximal Antarctic
123 sea-ice record covering the last ca. 145 kyrs. We present biomarker-based reconstructions of sea ice,
124 subsurface ocean temperature, total organic carbon (TOC) and biogenic silica (bSiO₂) content, as well
125 as diatom-based sea-ice concentration and summer sea surface temperature (SSST). This information
126 is complemented by reconstructions of sea ice, primary productivity and SSST records from a
127 neighboring core in the South Scotia Sea as well as numerically modeled sea ice, sea surface and
128 subsurface temperatures to track latitudinal shifts in the environmental development in the Atlantic
129 sector of the SO.

130 **2 Study area**

131 The Powell Basin (Fig. 1a) is a semi-isolated basin situated in the northwestern part of the Weddell
132 Sea. It has an area of approximately 5×10^4 km² and an average water depth of 3,300 km (Coren et al.,
133 1997; Viseras and Maldonado, 1999). The basin, enclosed by the Antarctic Peninsula to the west, the
134 South Scotia Sea to the north, the South Orkney Microcontinent to the east, and the Weddell Sea to
135 the South, is at present subject to the clockwise-circulating regime of the Weddell Gyre. As described
136 in Orsi et al. (1993) and Vernet et al. (2019), the gyre involves four main water masses, namely Antarctic
137 Surface Water, Warm Deep Water (WDW), Weddell Sea Deep Water (WSDW) and Weddell Sea
138 Bottom Water (WSBW; Fig. 1b). The Antarctic Surface Water generally consists of shelf waters formed
139 over the continental shelf, such as winter water, high salinity shelf water from brine rejection due to sea-
140 ice formation, and ice-shelf water from glacial melt. The shelf waters travel along the Weddell Sea
141 continental shelf via the Antarctic Coastal Current while denser shelf water cascades down and along
142 the continental slope as the Antarctic Slope Current (Deacon, 1937; Fahrbach et al., 1992; Jacobs,
143 1991; Thompson et al., 2018). The WDW originates from the warm, saline and low-oxygen Antarctic
144 Circumpolar Current that is advected and subsequently integrated into the gyre's circulation at its
145 eastern front (Orsi et al., 1993; 1995). Along the southern boundary of the Weddell Gyre, the WDW
146 upwells close to the Antarctic margin and mixes with the Antarctic Surface Water. The admixture cools
147 and becomes denser, giving rise to the formation of WSDW and WSBW water masses at deeper water
148 depths (Carmack and Foster, 1975; Dorschel, 2019; Huhn et al., 2008). In the Powell Basin, part of the
149 WSDW flows out into the Scotia Sea through channels on the western slope of the basin (namely Philip,
150 Bruce and Discovery Passages; Morozov et al., 2020). The remaining WSDW and a part of WSBW

151 navigate around the southern and eastern South Orkney Plateau, progressing northward via the Orkney
 152 Passage as AABW, while the residual WSBW recirculates within the Weddell Gyre (Fedotova and
 153 Stepanova, 2021; Gordon et al., 2001; Orsi et al., 1999).

154



155 Figure 1. a) Map of the study area showing the locations of marine sediment cores PS118_63-1 (yellow
 156 star), PS67/219-1 (red star) and EDML ice core (light blue circle) discussed in this paper. Mean winter and
 157 summer sea-ice extent (1981-2010; Fetterer et al., 2017) are illustrated by blue and yellow dotted lines,
 158 respectively. Map was adapted from the Norwegian Polar Institute's Qantarctica package using QGIS 3.28
 159 (Matsuoka et al., 2018). b) Diagram of the Weddell Gyre water masses with vertical temperature profiles
 160 collected near to our core sites in Powell Basin (-61.125°S, -47.675°W) and South Scotia Sea (-57.125°S, -
 161 42.375°W; World Ocean Atlas 18; Locarnini et al., 2018). Pathways of ocean currents (ACC: Antarctic
 162 Circumpolar Current – black; ACoC: Antarctic Coastal Current – grey) and water masses (ISW: Ice Shelf
 163 Water – light blue; HSSW: High Saline Shelf Water – blue; WDW: Warm Deep Water – green; WSDW:
 164 Weddell Sea Deep Water – red and WSBW: Weddell Sea Bottom Water – dark magenta) are represented by
 165 the colored arrows. AASW: Antarctic Surface Water, PB: Powell Basin, SOM: South Orkney Microcontinent.
 166

167 3 Materials and methods

168 3.1 Sediment core and age model

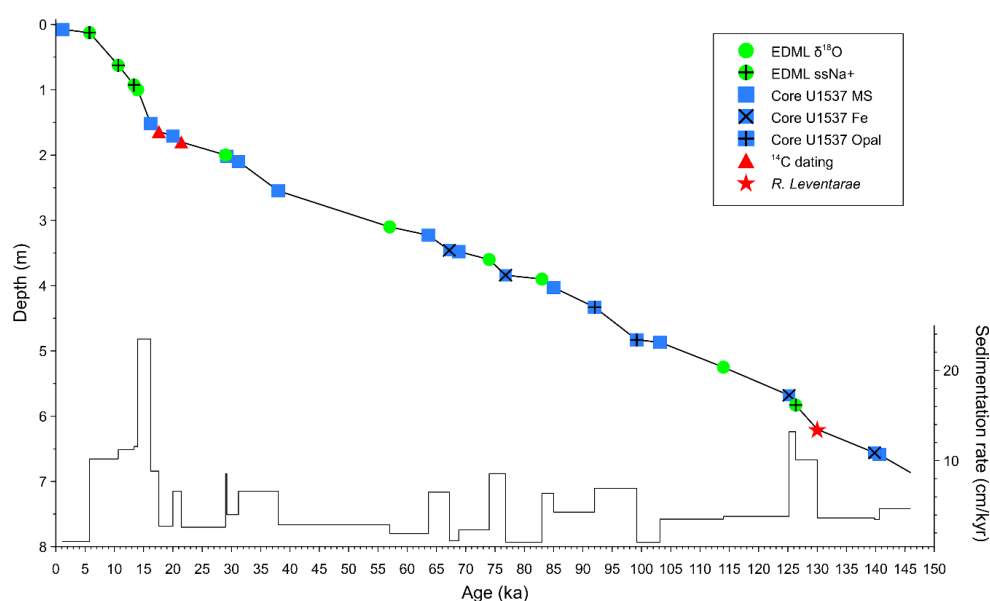
169 Gravity core PS118_63-1 was recovered from the Powell Basin during the RV *Polarstern* cruise
 170 PS118 to the Weddell Sea in 2019 (Fig. 1a; Table 1; Dorschel, 2019). Physical properties, such as
 171 magnetic susceptibility (MS) and wet-bulk density, were provided by Frank Niessen (shipboard data;
 172 Dorschel, 2019). The age model of core PS118_63-1 is based on ¹⁴C radiocarbon dates, the
 173 identification of the biostratigraphic marker *Rouxia leventerae*, as well as tuning against records from
 174 the EDML ice core ($\delta^{18}\text{O}$ and ssNa⁺) and nearby marine sediment core U1537 (MS, XRF-Fe and opal;
 175 Weber et al., 2022). Refer also to Fig. 2 and Supplementary Table S2 for the tie points. Our age model
 176 is further substantiated by age constraints of the uranium series disequilibrium, in particular the
 177 constant-rate-of-supply model for ²³⁰Th-excess (Geibert et al., 2019). Further details on the
 178 establishment of the age model and methods are provided in Supplement S1 and S2.

179

180 **Table 1. Locations and details of investigated and discussed cores.**

Station	Latitude	Longitude	Water depth / Elevation (m)	Recovery (m)	Data source
Marine sediment cores					
PS118_63-1	61° 07.421'S	47° 44.028'W	2626.5	6.88	this study
PS67/219-1	57° 13.22'S	42° 28.02'W	3619	20.71	this study; Xiao et al, 2016a; Xiao et al, 2016b
Ice core					
EDML	75°S	0°	2891		EPICA Community Members, 2006; Fischer et al, 2007

181



182

183 **Figure 2. Tie points used for the age-depth model of PS118_63-1 and sedimentation rates. EDML ice core**
 184 **data is indicated by green circles, marine core U1537 data is marked by navy blue square, and available**
 185 **AMS ¹⁴C dates and the biostratigraphic marker (*R. leventerae*) from core PS118_63-1 are depicted by red**
 186 **triangles (¹⁴C dates) and a red star (*R. leventerae*).**

187 **3.2 Bulk and organic geochemical analyses**

188 A total of 108 sediment samples, each with an approximate thickness of 1 cm, were collected from
 189 core PS118_63-1. These samples were then freeze-dried and homogenized using an agate mortar and
 190 pestle. All samples were stored in glass vials at -20 °C to prevent degradation. To analyze total organic
 191 carbon (TOC), about 0.1 g of sediment was treated with 500 μL of hydrochloric acid to remove any
 192 inorganic carbon, including carbonates. After the treatment, the TOC content was measured using a
 193 carbon-sulfur analyzer (ELTRA CS800). Routine analyses of standard sediments were conducted
 194 before and during each measurement yielding an error of ±0.02%. Biogenic opal was determined using
 195 the automated continuous wet-chemical leaching method prescribed in Müller and Schneider (1993)
 196 with an error of ±2 wt.%. For biomarker analyses, around 5-8 g of sediment were extracted and purified
 197 in accordance with well-established protocols (Belt et al., 2012; Lamping et al., 2021). Prior to
 198 extraction, internal standards, 7-hexylnonadecane (7-HND) and C₄₆-GDGT, were added for subsequent

199 quantification of HBIs and glycerol dialkyl glycerol tetraether (GDGT) lipids. The biomarkers were
200 extracted via ultrasonication (3 x 15 min) using DCM:MeOH (3 x 10 mL; 2:1 v/v) as solvent. Thereafter,
201 the extracts were fractionated via open-column chromatography, with SiO₂ as the stationary phase, with
202 the HBI-containing fractions eluted with 5 mL *n*-hexane and the GDGT fractions with 5 mL DCM:MeOH
203 (1:1 v/v).

204 Compound analyses of HBIs were performed using an Agilent 7890B Gas Chromatograph (GC;
205 fitted with a 30 m DB 1MS column; 0.25 mm diameter and 0.250 µm film thickness) coupled to an
206 Agilent 5977B Mass Selective Detector (MSD; with 70 eV constant ionization potential, ion source
207 temperature of 230°C). The GC oven temperature was first set to 60°C (3 min), then to 150°C (heating
208 rate of 15°C/min), and finally to 320°C (heating rate of 10°C/min), at which it was held for 15 min for the
209 analysis. Helium was used as the carrier gas. Specific compound identification was based on their
210 retention times and mass spectra characteristics (Belt, 2018; Belt et al., 2000).

211 Quantification of each biomarker was based on setting the manually integrated GC-MS peak area
212 relative to corresponding internal standards and instrumental-compound response factors. The
213 concentrations were subsequently corrected to the extracted sediment weight. For HBI quantification,
214 the molecular ions *m/z* 348 (IPSO₂₅) and *m/z* 346 (*z*-/*e*-trienes) were used in relation to its internal
215 standard 7-HND (*m/z* 266). Finally, all biomarker mass concentrations were normalized to the TOC
216 content of each sample. For calculating PIPSO₂₅, we adopted the equation as described in Vorrath et
217 al. (2019):

$$\text{PIPSO}_{25} = \text{IPSO}_{25} / (\text{IPSO}_{25} + (\text{phytoplankton marker} \times c)), \quad (1)$$

218 where *c* is the ratio between the mean concentrations of IPSO₂₅ and phytoplankton marker and
219 balances any significant offsets between both biomarker concentrations (Müller et al., 2011).

220 The GDGT fraction was dried (N₂) and redissolved in 120 µL hexane-isopropanol alcohol (99:1
221 v/v), followed by filtration through a polytetrafluoroethylene (PTFE) filter with 0.45 µm pore size
222 membrane. GDGT measurement was performed using an Agilent 1200 series high-performance liquid
223 chromatograph coupled to an Agilent 6120 atmospheric pressure chemical ionization mass
224 spectrometer. Identification of isoprenoid GDGTs (isoGDGTs) and branched GDGTs (brGDGTs) was
225 based on retention times and mass-to-charge ratios (isoGDGTs: *m/z* 1302, 1300, 1298, 1296 and 1292;
226 brGDGTs: *m/z* 1050, 1036 and 1022). The late eluting hydroxylated-GDGTs (OH-GDGTs) with
227 molecular ions *m/z* 1318, 1316 and 1314 were also determined during the scan of related isoGDGTs,
228 namely *m/z* 1300, 1298 and 1296, respectively (Liu et al., 2012a; 2012b). The relative abundances
229 were subsequently quantified relative to internal standard C₄₆ (*m/z* 744), instrumental response factors
230 and the amount of sediment extracted. Mass content of all GDGTs were normalized to the TOC content
231 of each sample.

232 The isoGDGT-based index, TEX₈₆^L (Eq 2) was calculated following Kim et al. (2010) while the
233 conversion to subsurface ocean temperature (OT; 0 - 200 m water depth; Eq 3) was conducted in
234 accordance to Hagemann et al. (2023):

$$\text{TEX}_{86}^L = \text{Log}_{10} \frac{[\text{isoGDGT-2}]}{[\text{isoGDGT-1}] + [\text{isoGDGT-2}] + [\text{isoGDGT-3}]} \quad (2)$$

$$\text{OT } (^\circ\text{C}) = 14.38 \times \text{TEX}_{86}^L + 8.93; \text{ with a calibration error of } \pm 0.6^\circ\text{C} \quad (3)$$

235 The OH-GDGT-based index, RI-OH' (Eq 4) and the OT estimation (Eq 5) were determined following Lü
 236 et al. (2015). In their study, they determined that the RI-OH' is significantly correlated with temperature
 237 compared to other indices such as TEX_{86} and RI-OH, producing a lower and less scattered residual sea
 238 surface temperature (SST) of $\pm 6^\circ\text{C}$.

$$\text{RI-OH}' = \frac{[\text{OH-GDGT-1}] + 2 \times [\text{OH-GDGT-2}]}{[\text{OH-GDGT-0}] + [\text{OH-GDGT-1}] + [\text{OH-GDGT-2}]} \quad (4)$$

$$\text{RI-OH}' = 0.0382 \times \text{OT } (^\circ\text{C}) + 0.1 \quad (R^2 = 0.75, n = 107, p < 0.01) \quad (5)$$

239 The index of relative contribution of terrestrial organic matter against that of marine input (branched-
 240 isoprenoid tetraether, BIT; Eq 6) was calculated based on Hopmans et al. (2004):

$$\text{BIT} = \frac{[\text{brGDGT-I}] + [\text{brGDGT-II}] + [\text{brGDGT-III}]}{[\text{Crenarchaeol}] + [\text{brGDGT-I}] + [\text{brGDGT-II}] + [\text{brGDGT-III}]} \quad (6)$$

241 Lastly, we utilize the ring index (RI; Eqs 7 - 9; Zhang et al., 2016) and methanogenic source indicator
 242 index (%GDGT-0; Eq 10; Inglis et al., 2015) to validate against possible non-thermal GDGT sources
 243 contribution:

$$\text{RI}_{\text{sample}} = 0 \times [\text{isoGDGT-0}] + 1 \times [\text{isoGDGT-1}] + 2 \times [\text{isoGDGT-2}] + 3 \times [\text{isoGDGT-3}] + 4 \times [\text{crenarchaeol}] + 4 \times [\text{regio. crenarchaeol}] \quad (7)$$

$$\text{RI}_{\text{calculated}} = -0.77 \times \text{TEX}_{86} + 3.32 \times (\text{TEX}_{86})^2 + 1.59 \quad (8)$$

$$|\Delta\text{RI}| = \text{RI}_{\text{calculated}} - \text{RI}_{\text{sample}} \quad (9)$$

$$\% \text{isoGDGT-0} = \frac{[\text{isoGDGT-0}]}{[\text{isoGDGT-0}] + [\text{Crenarchaeol}]} \times 100\% \quad (10)$$

244 3.3 Diatom analyses

245 41 smear slides were prepared for a quantitative diatom assemblage analysis at respective depths
 246 of the core. Between 400-600 diatom valves, inclusive of those from *Chaetoceros* resting spores
 247 (*Chaetoceros* rs), were counted in each sample to ensure statistical significance of the results. Diatoms
 248 were identified to species or species group level and, if possible, to forma or variety level. The presence
 249 of sea ice is inferred from the percentage of sea-ice indicating diatoms. A combined relative abundance
 250 of *Fragilariopsis curta* and *Fragilariopsis cylindus* (hereon referred to as *F. curta* gp) of >3% is used as
 251 a qualitative threshold to represent presence of WSI, while values between 1 and 3% estimates the

252 edge of maximum winter sea ice (Gersonde et al., 2003; 2005). Likewise, *Fragilariopsis obliquecostata*
253 is used to indicate summer sea ice (Gersonde and Zielinski, 2000).

254 We reconstructed WSI concentration (WSIC) by applying a marine diatom transfer function
255 developed by Esper and Gersonde (2014a; TF MAT-D274/28/4an). This transfer function consists of
256 274 reference samples from surface sediments in the Atlantic, Pacific and western Indian sectors of the
257 SO, with 28 diatom taxa and taxa groups, and an average of 4 analogs (Esper and Gersonde, 2014a).
258 The WSI estimates refer to September sea-ice concentration averaged over a period between 1981
259 and 2010 at each surface sediment site (National Oceanic and Atmospheric Administration, NOAA;
260 Reynolds et al., 2002; 2007). The reference dataset fits our approach as it uses a 1° by 1° grid, providing
261 a higher resolution than previously used, and giving a root mean square error of prediction of 5.52%
262 (Esper and Gersonde, 2014a).

263 The SSST was estimated using TF IKM-D336/29/3q (standard error of $\pm 0.86^{\circ}\text{C}$), comprising 336
264 reference samples from surface sediments in the Atlantic, Pacific and western Indian sectors of the SO,
265 with 29 diatom taxa and taxa groups, and a 3-factor model calculated with quadratic regression (Esper
266 and Gersonde, 2014b). The SSST estimates refer to summer (January-March) temperatures at 10 m
267 water depth averaged over a time period from ≤ 1900 to 1991 (Hydrographic Atlas of the Southern
268 Ocean; Olbers et al., 1992). The Hydrographic Atlas of the Southern Ocean was used because it
269 represents an oceanographic reference dataset least influenced by the recent warming in the SO (Esper
270 and Gersonde, 2014b).

271 **3.4 Comparison with other proxy records**

272 The EDML ice core and the marine sediment core PS67/219-1 are used in this study for regional
273 comparison due to proximity of both cores to our core site (Fig. 1a; see also Table 1 for details). Water
274 isotope ($\delta^{18}\text{O}$) and ssNa^+ records of the EDML ice core were investigated by EPICA Community
275 Members (2006) and Fischer et al. (2007), respectively. Marine sediment core PS67/219-1, retrieved
276 from the South Scotia Sea, is located south of the Polar Front and just north of the modern-day winter
277 sea-ice extent. This core offers data on sea ice, SSST and biogenic opal, which extend at least to the
278 LIG period, making it suitable for comparison with core site PS118_63-1. The chronology and biogenic
279 opal data of core PS67/219-1 was described and published in Xiao et al. (2016b), while investigations
280 on sea-ice reconstruction and SSST for the last 30 ka BP are presented in Xiao et al. (2016a). We
281 further extend the WSIC and SSST records, back to 150 ka BP, using the transfer functions TF MAT-
282 D274/28/4an and TF IKM-D336/29/3q, respectively (Esper and Gersonde, 2014a; 2014b).

283 **3.5 Comparison with simulations from climate model(s)**

284 Here, we also analyze model-simulated sea ice, SST and OT estimates for further comparison and
285 evaluation against our proxy results. In this respect, the strength of our modeling approach is twofold.
286 First, the model shall provide reasonable coverage of our intended studied time slices, mainly 6, 21,
287 125, 128 and 140 ka BP. Second, the model's sensitivity to various climate forcings and boundary
288 conditions across the Quaternary and the entire Cenozoic era must be known. To this end, the
289 Community Earth System Models (COSMOS; Jungclaus et al., 2006) is chosen over other climate

290 models due to its proven track record. For example, the simulation ensemble that has been produced
291 over the years with COSMOS is extensive and not available from international modeling initiatives like
292 the Paleoclimate Modeling Intercomparison Project (PMIP; e.g., Braconnot et al., 2012). Likewise, the
293 model has reproduced various aspects of reconstructed paleoclimate data (see Supplement S3.1 for a
294 list of paleo-studies using the COSMOS model), is shown to be sensitive to paleogeography and climate
295 forcing, and is being characterized by a large Climate and Earth System Sensitivity (Haywood et al.,
296 2013; Stepanek and Lohmann, 2012). Additionally, COSMOS has been proven useful for the study of
297 both warmer (Pfeiffer and Lohmann, 2016) and colder (Zhang et al., 2013; 2017) climates than today
298 and supported research in sometimes very interdisciplinary frameworks (e.g., Guagnin et al., 2016;
299 Klein et al., 2023). For some of the periods relevant here – Holocene, Last Glacial Maximum, LIG –
300 standalone applications of the model are documented (e.g., Pfeiffer and Lohmann, 2016; Wei and
301 Lohmann, 2012; Zhang et al., 2013). More importantly, results from COSMOS have been extensively
302 compared to other models, particularly within the framework of the PMIP, with a focus on the
303 Holocene (Dallmeyer et al., 2013; 2015; Varma et al., 2012) and the Last Interglacial (Bakker et al.,
304 2014; Jennings et al., 2015; Lunt et al., 2013). A relevant inference from comparing PMIP3-class models
305 is that, from the viewpoint of model performance in the SO, COSMOS has shown to be among the
306 models with a comparably minor warm bias in SST (see Fig. 4e and f in Lunt et al., 2013). This makes
307 COSMOS particularly suitable for the studies of ocean temperatures and sea ice around the Weddell
308 Sea. We refer to additional discussion on the rationale for choosing COSMOS over the PMIP models
309 in our study in the Supplement S3.3. Additionally, we also provide an in-depth comparison and
310 evaluation of the simulated results from PMIP3 and PMIP4 ensemble models, within the context of our
311 study, and agreement between COSMOS and PMIP ensemble models in the Supplement S3.4.

312 3.5.1 *Community Earth System Models*

313 In our study, the model data is derived from climate simulations performed with COSMOS. The
314 model's atmospheric module is the fifth generation of the European Centre for Medium-Range Weather
315 Forecasts' Model (ECHAM5), a model of the general circulation of the atmosphere with a spectral
316 dynamical core developed at the Max Planck Institute for Meteorology in Hamburg (Stevens et al.,
317 2013). In our model setup, the ECHAM5 is employed at a truncation of T31, corresponding to a spatial
318 resolution of approximately $3.75^\circ \times 3.75^\circ$, or 375 km at the equator. The atmospheric column is
319 discretized at a resolution of 19 vertical hybrid sigma-pressure levels. The ECHAM5 also encompasses
320 a land surface component (JSBACH) that represents multiple land cover classification types (Loveland
321 et al., 2000; Raddatz et al., 2007). We employ JSBACH's capability to reflect vegetation dynamics
322 (Brovkin et al., 2009) in the course of climate simulations. In our setup, we consider eight different plant
323 functional types that the model adapts in response to changes in the simulated climate, thereby
324 reflecting important feedback processes between vegetation and climate in our simulations. The ocean
325 module is the Max Planck Institute Ocean Model (MPIOM; Marsland et al., 2003), employed at 40
326 unevenly spaced pressure levels with a bipolar curvilinear GR30 grid that has a formal resolution of
327 $1.8^\circ \times 3.0^\circ$. This enables the horizontal resolution to reach grid cell dimensions that are as small as 29
328 km at high latitudes. Sea ice computation is based on dynamic-thermodynamic processes with viscous-

329 plastic rheology and follows the formulation by Hibler (1979). Various parameterizations improve the
330 representation of small-scale ocean dynamics in the simulations. For additional information about the
331 parameterizations utilized in our model setup and the steps taken to create geographic setups to apply
332 the model in paleoclimatological research, see, for example, Stepanek et al. (2020) and references
333 therein.

334 3.5.2 COSMOS simulation settings

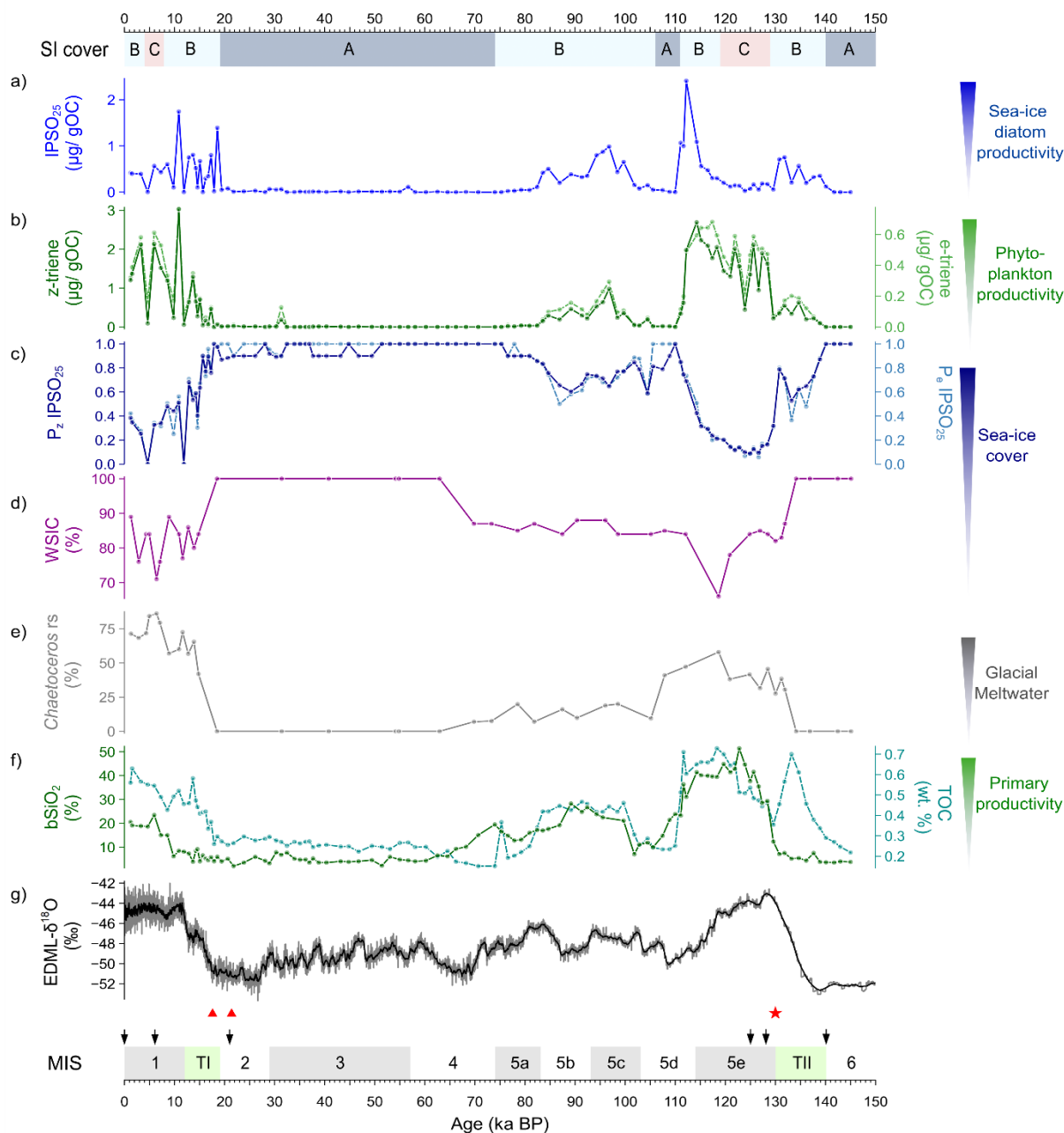
335 The simulation ensemble consists of a pre-industrial reference state (simulation *piControl*, 1850
336 CE; Wei and Lohmann, 2012), a Holocene climate (simulation *mh6k*, 6 ka BP; Wei and Lohmann, 2012),
337 an LGM state (simulation *lgm21k*, 21 ka BP; Zhang et al., 2013), two time-slices of the LIG, one for
338 conditions at 125 ka BP (simulation *lig125k*) and one for conditions at 128 ka (simulation *lig128k*), and
339 a Penultimate Glacial Maximum (PGM) climate (simulation *pgm140k*). In order to filter out short-term
340 climate variability on interannual and multidecadal time scales, and to derive average climatic conditions
341 that are representative of the respective Quaternary time-slice, we average the modeled climate state
342 over a period of 100 model years. For interglacial climates we employ a modern geography. The
343 boundary conditions for the Last and Penultimate Glacial Maximum have been set up for a study by
344 Zhang et al. (2013) based on the PMIP3 modeling protocol. Details of the ice-sheet reconstruction, that
345 is a blend of ICE-6G v2.0 (Argus and Peltier, 2010), ANU (Lambeck et al., 2010) and GLAC-1a (Tarasov
346 et al., 2012), are described by Abe-Ouchi et al. (2015). For further details on the climate states and
347 simulation configurations, we refer to S3.2 and Supplementary Table S3, respectively in the
348 Supplement. For analysis purposes, the climate model output is interpolated from the native grid of the
349 ocean model to a regular resolution of $0.25^\circ \times 0.25^\circ$, in order to preserve the geographic features of the
350 ocean model. Additionally, we also derived climate model data specifically tailored to the two marine
351 core sites discussed in this paper, achieving this through interpolating relevant climate fields to the
352 geographic coordinates of each core using a nearest-neighbor interpolation algorithm. Any reference
353 to the modeled sea-ice edges in this publication specifies the isoline of 15% of sea-ice cover.

354 4 Results

355 4.1 HBIs

356 The concentration of the sea-ice biomarker (IPSO₂₅; Fig. 3a) in core PS118_63-1 varies
357 significantly between 0 and 2.41 $\mu\text{g/g}$ OC. Peak concentration is found at ca. 112 ka BP, while very low
358 concentrations are noted throughout MIS 2-4, 5d, 5e and 6. Moderate to low concentrations are
359 observed during MIS 1 and through both terminations. The concentration of the ice marginal-open water
360 phytoplankton biomarkers varies between 0 - 3.03 $\mu\text{g/g}$ OC (z-triene) and 0 - 0.76 $\mu\text{g/g}$ OC (e-triene;
361 Fig. 3b). Higher concentrations are observed at MIS 1 and 5e, while lower concentrations are noted
362 throughout MIS 2-4, 5d and 6. In our investigation, we utilized both z- and e-trienes, respectively, to
363 calculate the semi-quantitative spring/summer sea-ice indices ($P_{z/e}\text{IPSO}_{25}$). This combined use of
364 biomarkers, indicative of ice marginal-open water conditions and IPSO₂₅, helps to circumvent
365 ambiguous interpretations especially when dealing with scenarios of permanent sea ice and open ocean

366 conditions. Our P_z IPSO₂₅ index ranges between 0.09 and 1, while the P_e IPSO₂₅ index varies from 0.06
 367 to 1 (Fig. 3c). Instances, where both values of IPSO₂₅ and z-/e-triene are zero, the P_z / P_e IPSO₂₅ index is
 368 assigned a value of 1, indicating permanent ice cover. Both index profiles presented a similar trend (r
 369 = 0.98), with higher values (>0.8) throughout MIS 2-4, 5d and 6, while reduced values noted for MIS 1
 370 and 5e. Notably, the lowest P_z / P_e IPSO₂₅ values (<0.2) are observed during MIS 5e, specifically between
 371 119 and 128 ka BP, signifying a distinct decline in sea ice and more open ocean conditions during this
 372 time interval. Comparable low P_z / P_e IPSO₂₅ values are also observed around 4 and 12 ka BP.



373
 374 **Figure 3. Multiproxy analyses of sea-ice conditions in Powell Basin, reconstructed from marine sediment**
 375 **core PS118_63-1. Sea-ice (SI) cover scenarios: A - permanent sea-ice cover (dark blue), B - dynamic sea-**
 376 **ice cover (light blue) and C - minimal sea-ice cover (light red). From top to bottom: a) HBI-based sea ice**
 377 **biomarker (IPSO₂₅), b) HBI-based phytoplankton biomarkers (z-/e-trienes), c) Phytoplankton-IPSO₂₅ index**
 378 **(PIPSO₂₅), d) Diatom-based winter sea-ice concentration (WSIC), e) Glacial meltwater indicator**
 379 **(*Chaetoceros* resting spores) and f) Biogenic opal (bSiO₂), and total organic carbon (TOC). Atmospheric**
 380 **temperature is implied by g) the δ¹⁸O record from the EDML ice core. AMS ¹⁴C dates are marked with red**
 381 **triangles, the biostratigraphic marker (*R. leventerae*) is indicated by the red star. The black arrows**

382 delineated the time-slices for the model simulations in this study. MIS stages are depicted in alternating
383 grey (odd) and white (even) shades, while the terminations TI and TII are shown in green.

384 4.2 GDGTs

385 Downcore OT estimates using the RI-OH' index cover a temperature range between -2.5 and
386 1.0°C (Fig. 4g) while TEX₈₆^L-derived OT fluctuates between -2.6 and 1.0°C (Supplementary Fig. S5a).
387 These GDGT-based OTs likely reflect (mean) annual ocean temperature between the water depths of
388 0 and 200 m (Hagemann et al., 2023; Kim et al., 2012; Liu et al., 2020), and this seems to be
389 corroborated by the modern-day vertical ocean temperature profile nearby core site PS118_63-1 (Fig.
390 1b). Certainly, these minimum temperatures of less than -1.9°C – freezing temperature of seawater –
391 need to be considered with caution due to factors influencing the ocean temperature calibration, for
392 example, bias from terrestrial input, water depth, use of satellite-assigned ocean temperature below the
393 freezing point of seawater and inadequate samples from polar areas (Fietz et al., 2020; Xiao et al.,
394 2023). Nevertheless, both OT proxies consistently indicate a cold-water subsurface regime (0 – 200 m;
395 <1°C) with a 0-2°C temperature fluctuation, and no significant glacial/interglacial variability over the last
396 145 kyrs. We further note that the RI-OH'-based OTs fluctuate within the error range of the temperature
397 calibration based on a global surface sediment dataset (Lü et al., 2015) and call for attention when
398 interpreting OT variability. Calculation of terrestrial originated-GDGT (i.e. BIT) and isoGDGT-related
399 indices (i.e. %isoGDGT-0 and ΔRI; Supplementary Fig. S5b-e) reveals the presence of potential non-
400 thermal influences on the TEX₈₆^L index, which may lead to bias in the temperature reconstruction (see
401 also S4 in the Supplement). In light of the non-thermal influences on TEX₈₆^L, we have decided not to
402 further discuss on the TEX₈₆^L-derived OT in this paper. Concerning the RI-OH' approach, the presence
403 of OH-GDGT has, thus far, only been observed within the cultivated marine thaumarchaeal group I.1a
404 (Pitcher et al., 2011; Liu et al., 2012b; Elling et al., 2014; 2015). Its absence in the terrestrial
405 thaumarchaeal group I.1b (Sinninghe Damsté et al., 2012) suggests a predominantly planktic origin (Lü
406 et al., 2015). While both isoGDGTs and OH-GDGTs are derived from the phylum *Thaumarchaeota*,
407 variances in their ring composition indicate that the OH-GDGTs may be biosynthesized from different
408 source organisms or differing conditions (Liu et al., 2012b). Additionally, previous studies compared the
409 relationship between various GDGT-based indices (i.e. RI-OH, RI-OH', TEX₈₆ and TEX₈₆^L) and
410 temperature, and determined that the RI-OH'-temperature relationship shows the most significant
411 correlation in cold-water (<15°C) regions, making the RI-OH' a robust temperature proxy for the
412 (sub)polar regions (Lü et al., 2015; Lamping et al., 2021; Park et al., 2019; Fietz et al., 2020). Therefore,
413 we suggest that the RI-OH' index holds promise as a potential OT proxy for our study site. However,
414 further work on the distribution of OH-GDGT and calibration studies are still essential to enhance the
415 applicability of RI-OH' as a (paleo)temperature proxy.

416 4.3 Diatoms

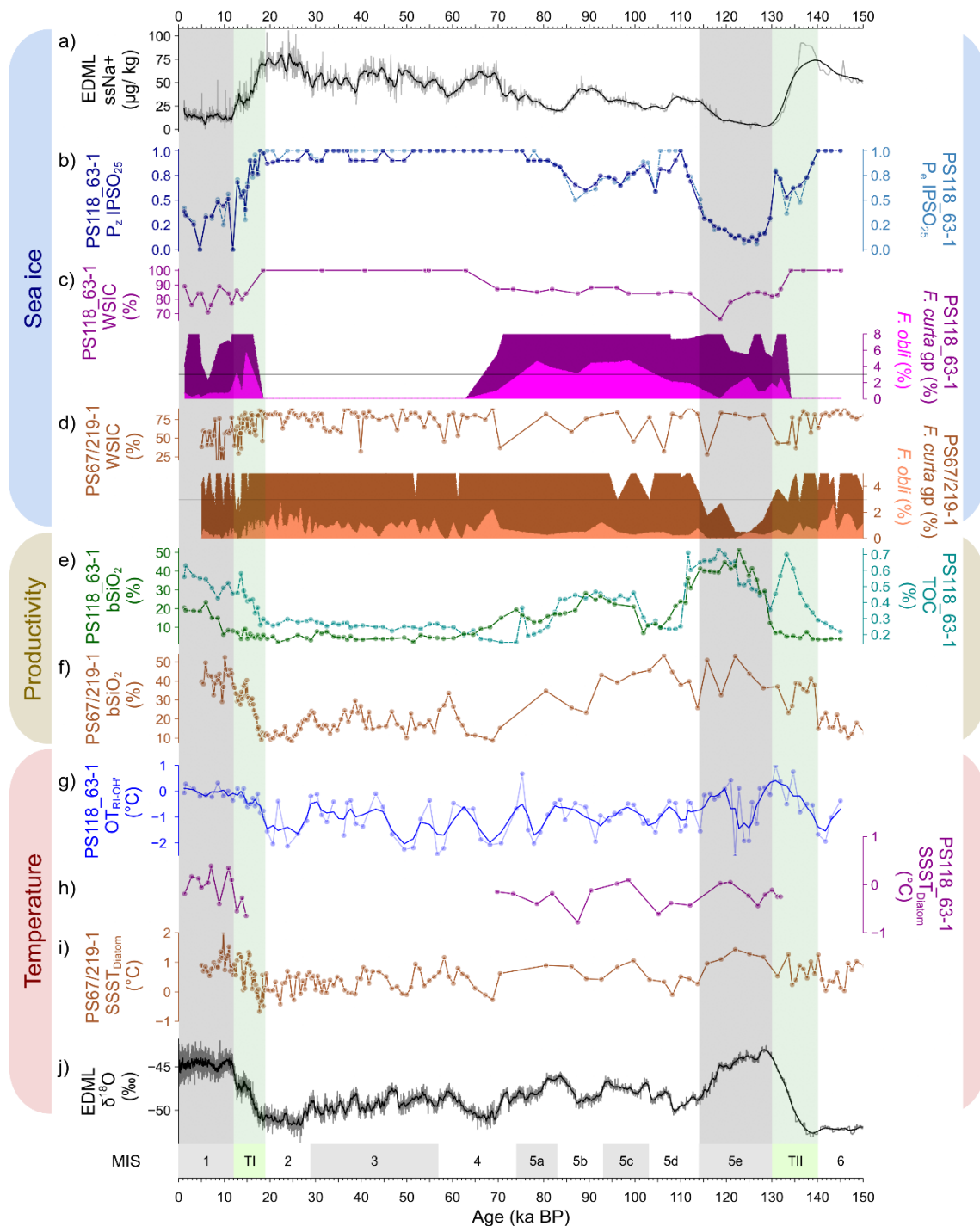
417 The diatom-based data for cores PS118_63-1 and PS67/219-1 are presented in Fig. 4c and d. For
418 core PS118_63-1 from the Powell Basin, the relative abundance of sea ice-related diatoms ranges
419 between 2 and 39% for *F. curta* gp, and from 0 to 6% for *F. obliquocostata*. The relative abundance of
420 diatoms between ca. 15 and 70 ka BP, and before 131 ka BP, is rare/absent (Fig. 4c). Such cases

421 generally indicate the presence of permanent sea ice over the core site (Zielinski and Gersonde, 1997).
422 We, therefore, assign the diatoms' relative abundance as 0, and WSIC as 100%, to above-mentioned
423 time intervals (i.e., MIS 2 - 4 and 6). The abundance of *F. curta* gp is noted to be above the 3% threshold
424 (indicative of presence of WSI) throughout the remaining time periods – except at 6 ka BP, where the
425 lowest abundance (2%) is observed. A relative abundance of *F. obliquocostata* around the 3% threshold
426 indicates a dynamic summer sea-ice edge over the area during MIS 1 and 5. The WSIC across the rest
427 of the time frame, namely MIS 1 and 5, is generally high (>75%) with a couple of lower WSIC observed
428 at ca. 6 ka BP (71%) and at 119 ka BP (66%). The abundance of *Chaetoceros* resting spores
429 (*Chaetoceros* rs) varies between 0 and 86%, with higher values noted during MIS 1 and 5e (Fig. 3e).
430 Such increases in the abundance of the *Chaetoceros* rs imply the presence of glacial meltwater at the
431 core location (Crosta et al., 1997). The diatom-derived SSST – typically indicating summer ocean
432 temperature between the water depth of 0 and 10 m – covers a temperature range between -0.8 and
433 0.4°C (Fig. 4h), and describes a cold-water region during MIS 1 and 5, similar to the RI-OH'-derived OT
434 (Fig. 4g).

435 To the north in the South Scotia Sea, core PS67/219-1 documents an overall lower percentage of
436 sea ice-related diatoms (Fig. 4d). Similar to core PS118_63-1, the relative abundance of *F. curta* gp
437 (0.5-20%) is noted to be mostly above the 3% threshold, indicating presence of WSI over the region,
438 with higher abundance observed for MIS 2 and 3, and lowest abundance (<1%) observed during MIS
439 5e. However, the relative abundance of *F. obliquocostata* for core PS67/219-1 remains below the 3%
440 threshold, between 0 and 3%, suggesting a lack of summer sea ice over the core site. The percentage
441 of WSIC in the South Scotia Sea is also lower than that of Powell Basin, with a record of 37-82%. The
442 diatom-based SSST documents a SSST range of -0.7 to 2°C, with colder SSST registered during MIS
443 2 and 3, and warmer SSST noted during MIS 1 and 5e (Fig. 4i).

444 **4.4 TOC and Biogenic opal**

445 In this study, both TOC and biogenic opal (Fig. 3f) are interpreted to reflect primary productivity (r
446 = 0.65). The TOC content varies between 0.2 and 0.7% while biogenic opal ranges from 2 to 51%.
447 Highest productivity is observed during MIS 1 and 5e, indicative of favorably warmer conditions that
448 promote primary productivity blooms at the core location. A rather moderate productivity level is
449 observed between MIS 5a to c, while lowest values are noted for MIS 2-4, 5d and 6. Both profiles also
450 exhibit some differences. For example, peak biogenic opal occurs around 124 ka BP whilst peak TOC
451 is recorded at 119 ka BP. We also observe a more pronounced increase in the TOC content during the
452 terminations than in the biogenic opal content. This is likely due to greater input from non-siliceous
453 organisms, such as archaeal, bacterial and terrestrial input (see Supplementary Fig. S4).



454

455 **Figure 4. Regional sea ice, productivity and temperature variability in the South Atlantic sector of the**
 456 **Southern Ocean as inferred from EDML ice core, Powell Basin (PS118_63-1) and South Scotia Sea**
 457 **(PS67/219-1). For sea ice: a) sea-ice estimation (ssNa+; black) from EDML ice core, b) HBI-based sea ice**
 458 **indicator (P_zIPSO₂₅ – dark blue; P_eIPSO₂₅ – dotted light blue), c) diatom-based winter sea-ice concentration**
 459 **(WSIC – dark magenta), *F. curta* gp – dark magenta), *F. obliquocostata* (*F. obli* – light**
 460 **magenta) from PS118_63-1, and d) diatom-based WSIC (brown), *F. curta* gp (*F. curta* gp – brown), *F.*
 461 ***obliquocostata* (*F. obli* – light brown) from PS67/219-1. For productivity: e) biogenic opal (bSiO₂ – dark**
 462 **green) and total organic carbon (TOC – dotted light green) from PS118_63-1 and f) bSiO₂ (brown) from**
 463 **PS67/219-1. For temperature: g) RI-OH'-derived subsurface ocean temperature with three-point smoothing**
 464 **(OT_{RI-OH'} – navy blue) and h) summer sea surface temperature (SSST_{Diatom} – dark magenta) from PS118_63-**
 465 **1, i) SSST_{Diatom} (brown) from PS67/219-1 and j) EDML water stable isotope record (δ¹⁸O – black). The 3%**
 466 **threshold for diatom species relative abundance is indicated by a black horizontal line. MIS stages are**
 467 **depicted in alternating grey (odd) and white (even) shades, while the terminations TI and TII are shown in**
 468 **green. For the full *F. curta* gp abundance data, refer to the relevant datasets in Pangaea.****

469 4.5 Sea-ice conditions – a multiproxy approach

470 Using a multiproxy approach, our analysis of the data from core PS118_63-1 provides a
471 continuous glacial-interglacial sea-ice history in the Powell Basin since the PGM. We distinguish three
472 different sea-ice scenarios spanning the last 145 kyrs (Fig. 3).

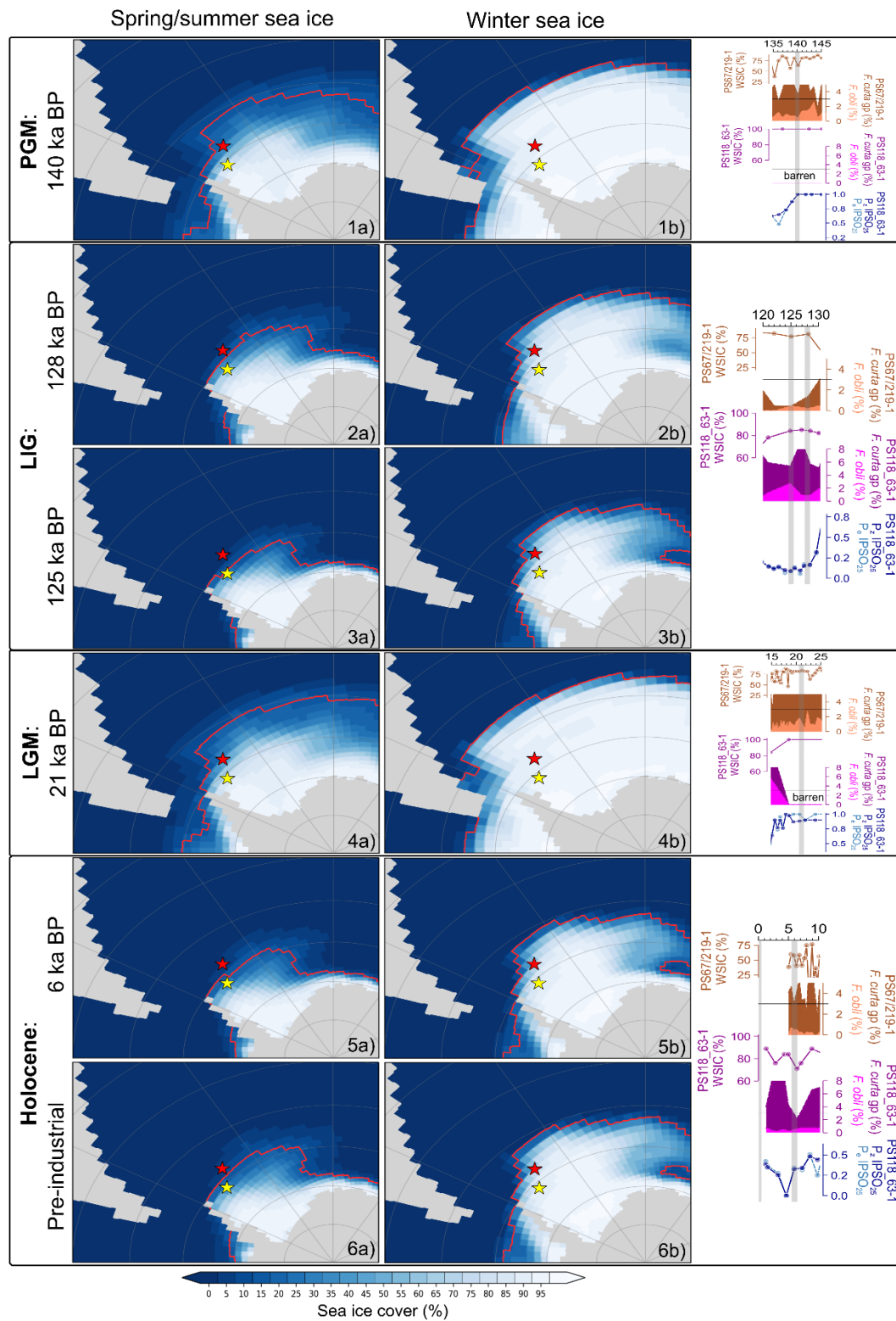
473 *A) Perennial sea-ice cover.* This scenario is characterized by remarkably low (sea ice) diatom
474 abundances, minimum IPSO₂₅ and HBI-triene concentrations, as well as minimum bSiO₂ and TOC
475 contents. We deduce the presence of maximum WSIC and spring/summer sea ice (PIPSO₂₅)
476 cover. These results indicate a glacial setting, with our core site situated under a perennial sea ice
477 or ice-shelf cover suppressing primary production in the water column. Such a scenario persisted
478 throughout the glacial periods MIS 2-4, MIS 6, and during MIS stadial 5d.

479 *B) Dynamic sea-ice cover.* This scenario is described by fluctuations in each of the proxy profiles,
480 in particular WSIC, PIPSO₂₅, HBI-trienes, bSiO₂ and TOC contents. These records reflect the
481 dynamic nature of sea-ice conditions over our core site, with varied primary production at different
482 time intervals. This scenario is prevalent during periods of climate transition, such as terminations
483 I and II, and during MIS 1 and 5a-c.

484 *C) Minimal (winter-only) sea-ice cover.* This scenario is denoted by a considerably reduced sea-
485 ice diatom (IPSO₂₅) production, WSIC and PIPSO₂₅, coupled with high phytoplankton productivity
486 (HBI-trienes), bSiO₂ and TOC contents. These findings suggest that our core site experienced ice-
487 free or winter-only ice conditions, permitting enhanced primary production in the water column.
488 This scenario occurs in short time intervals within the MIS 1 and MIS 5e.

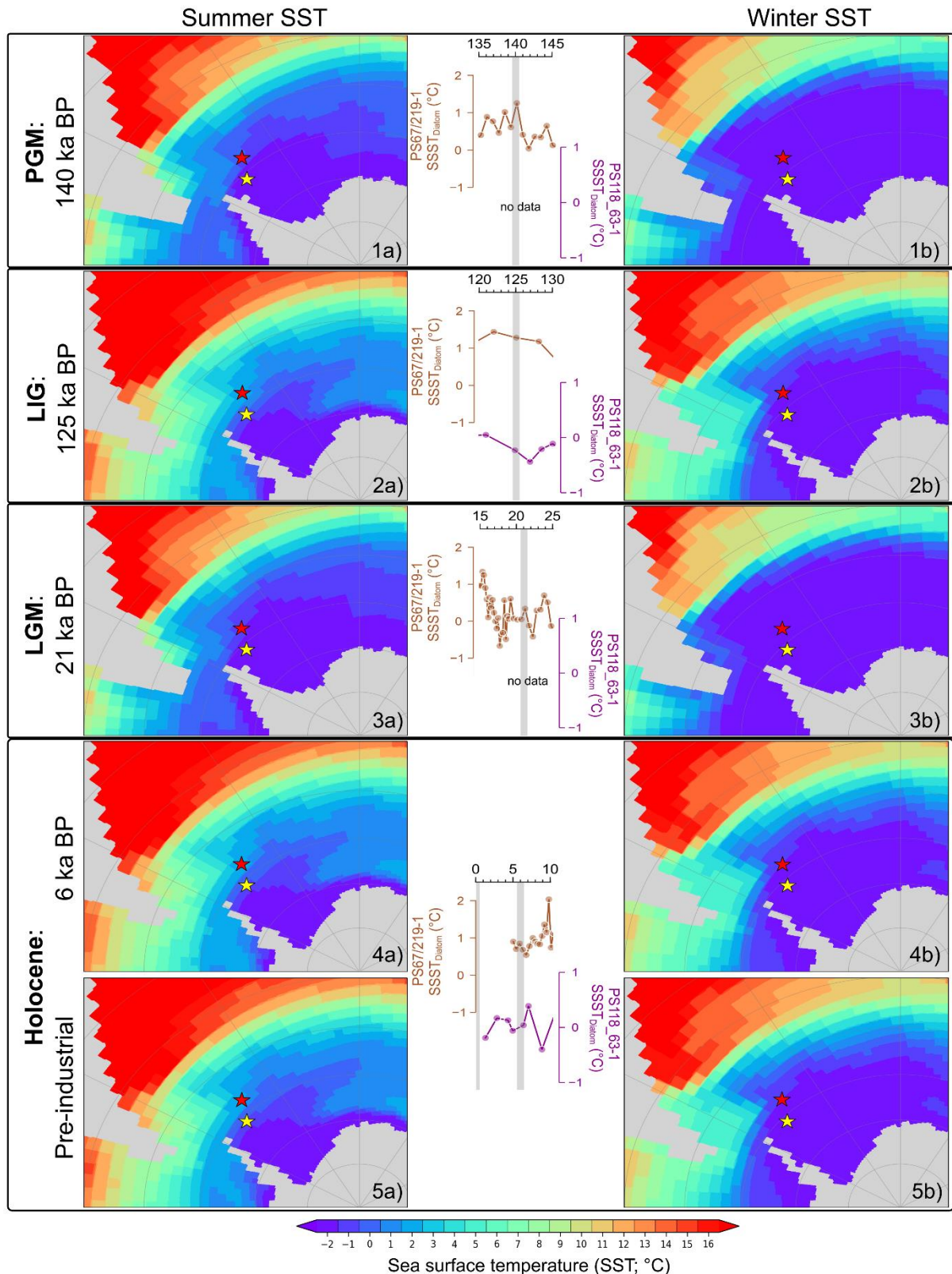
489 4.6 Inferences from COSMOS simulations

490 Covering the Atlantic sector of the SO, our model-simulated sea ice, SST and OT (at 220 m water
491 depth) glacial-interglacial time-slices cover the PGM at 140 ka BP, LIG at 128 (sea ice only) and 125
492 ka BP, LGM at 21 ka BP, Holocene at 6 ka BP and pre-industrial (Fig. 5 - 7). In Fig. 5, the left column
493 (Fig. 5a) shows the simulated sea-ice cover/extent for the spring/summer seasons (NDJFMA, this
494 averaging period considers the time lag in sea-ice extent vs. spring/summer temperature evolution)
495 while the right column (Fig. 5b) illustrates the simulated sea-ice cover/extent for the winter (ASO)
496 season. In general, a greater sea-ice cover is observed during winter than spring/summer for each time-
497 slice. During the glacial periods, the model highlights a northward expansion of the sea-ice extent
498 beyond both marine core sites (PGM: Fig. 5.1; LGM: Fig. 5.4). At the more southern site (Powell Basin;
499 core PS118_63-1), the modeled glacial sea-ice cover varies between ~93 to 94% (winter) and ~79 to
500 82% (spring/summer), while at the more northern site (South Scotia Sea; core PS67/219-1), sea-ice
501 cover varies around ~91% (winter) and ~26 to 34% (spring/summer). In contrast, during the
502 interglacials, fluctuations in sea-ice extent are more pronounced between seasons. WSI extent is
503 observed to be located north of both core sites (Fig. 5.2b, 5.3b, 5.5b and 5.6b), with the WSI cover
504 ranging between ~86 and 89% at core site PS118_63-1, and ~52 to 69% at core site PS67/219-1.
505 During spring/summer, the sea-ice extent retreats to a latitude between both sites (Fig. 5.2a, 5.3a, 5.5a
506 and 5.6a), with the spring/summer sea-ice cover varying from ~31 to 35% at core site PS118_63-1 and
507 between ~0 and 4% at core site PS67/219-1.



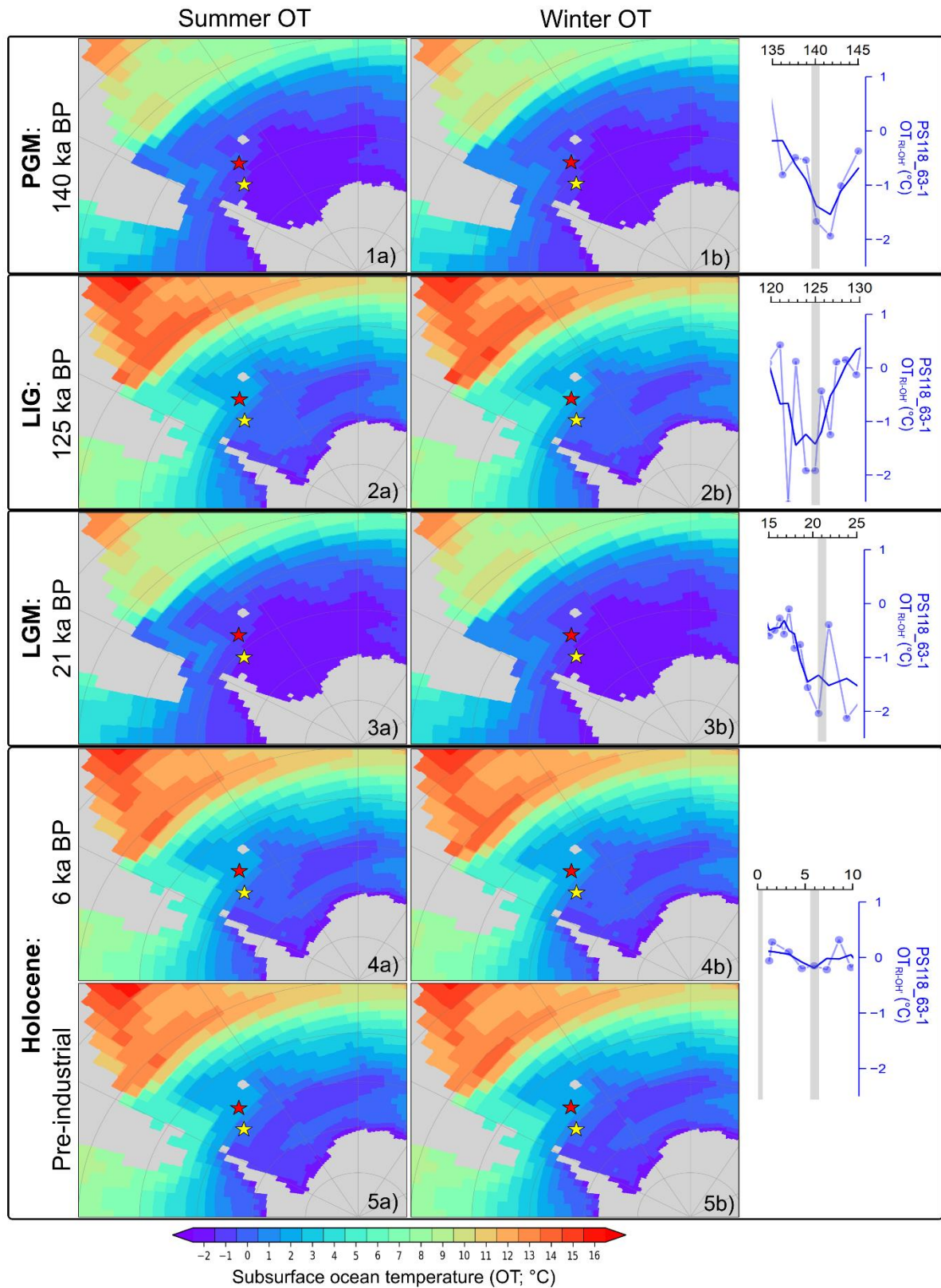
508
 509
 510
 511
 512
 513
 514

Figure 5. Model-simulated mean a) spring/summer (NDJFMA) and b) winter (ASO) sea-ice cover for the various time slices: 1) PGM: 140 ka BP, 2) LIG: 128 ka BP, 3) LIG: 125 ka BP, 4) LGM: 21 ka BP, 5) mid-Holocene: 6 ka BP and 6) Pre-industrial. The red line depicts the sea-ice extent and is defined as the isoline of 15% sea ice coverage. Location of marine sediment cores is indicated with stars: PS118_63-1 (yellow) and PS67/219-1 (red). Proxy-derived winter sea-ice concentration (WSIC), sea ice-related diatom abundance and spring/summer sea ice (PIPSO₂₅) for each time slice are shaded in grey.



515

516 **Figure 6. Model-simulated mean a) summer (DJF) and b) winter (JJA) sea surface temperature (SST) for**
 517 **the various time slices: 1) PGM: 140 ka BP, 2) LIG: 125 ka BP, 3) LGM: 21 ka BP, 4) mid-Holocene: 6 ka BP**
 518 **and 5) Pre-industrial. Marine sediment cores, PS118_63-1 (yellow) and PS67/219-1 (red), are indicated by**
 519 **the colored stars. Diatom-based summer sea surface temperature (SSST_{Diatom}) for the respective time slice**
 520 **is highlighted in grey.**



521

522 **Figure 7. Model-simulated mean a) summer (DJF) and b) winter (JJA) subsurface ocean temperature (OT;**
 523 **220 m water depth) for the various time slices: 1) PGM: 140 ka BP, 2) LIG: 125 ka BP, 3) LGM: 21 ka BP, 4)**
 524 **mid-Holocene: 6 ka BP and 5) Pre-industrial. Marine sediment cores are presented in colored stars:**
 525 **PS118_63-1 (yellow) and PS67/219-1(brown). Biomarker-based ocean temperature with three-point**
 526 **smoothing (OT_{RI-OH^+}) for the respective time slice is indicated by the grey shadings.**

527 For the SST and OT, the left columns (Fig. 6a and 7a) represent the summer (DJF) temperature,
528 and the right columns (Fig. 6b and 7b) depicts the winter (JJA) temperatures, respectively. The
529 simulated-SST (Fig. 6) appears similar to that of the modeled sea-ice output. In general, widespread,
530 low SST, close to the freezing point of seawater (that is approximately -1.9°C at salinity values modeled
531 in the SO in our simulations), is exhibited across all time-slices during winter (Fig. 6b), while in summer
532 (Fig. 6a), low SST mainly occurs in the Weddell Sea and along the coast of the Antarctic continent. For
533 instance, at the core site PS118_63-1 in Powell Basin, Weddell Sea, there is no observed difference in
534 SST between winter and summer during the glacial periods PGM (Fig. 6.1) and LGM (Fig. 6.3). Both
535 sites were surrounded by sea ice during these periods (Fig. 5.1 and 5.4). However, in interglacials, a
536 seasonal SST cycle of $\sim 1^{\circ}\text{C}$ is noted in the basin (Fig. 6.2, 6.4 and 6.5). In contrast, at the more northern
537 core site PS67/219-1, the model estimates a seasonal SST cycle of $\sim 1^{\circ}\text{C}$ during the glacial periods
538 (Fig. 6.1 and 6.3) and $\sim 3.4^{\circ}\text{C}$ during the interglacial (Fig. 6.2, 6.4 and 6.5). Moreover, the modeled
539 climate states are characterized by spatial SST gradients between the two core locations of between
540 0°C (glacial) and $\sim 0.4^{\circ}\text{C}$ (interglacial) during winter. For summer SST, the gradient between the two
541 core locations varies between $\sim 1^{\circ}\text{C}$ (glacial) and $\sim 2.8^{\circ}\text{C}$ (interglacial). As for the simulated OT, the
542 model displays a ~ 1.6 and $\sim 3^{\circ}\text{C}$ glacial-interglacial variation at core sites PS 118_63-1 and PS67/219-
543 1, respectively, but no appreciable OT change is observed between the winter and summer seasons of
544 each time slices (Fig. 7). The model also reveals a spatial OT gradient between both marine core sites
545 of $\sim 0.7^{\circ}\text{C}$ (glacial) and $\sim 2.1^{\circ}\text{C}$ (interglacial).

546 **5 Discussion**

547 **5.1 Regional sea ice and oceanic conditions**

548 *5.1.1 Penultimate Glacial Maximum – Termination II*

549 Our records show that during the PGM, the Powell Basin (core PS118_63-1) remained under a
550 layer of persistent (sea) ice cover, as evidenced by a 100% WSIC and peak PIPSO₂₅ values inferred
551 from the absence of diatoms, alongside notable reductions in IPSO₂₅ and HBI-triene concentrations
552 (see also Sect 4.1 and 4.3). This coincided with the lowest levels of primary production reflected in the
553 biogenic opal and TOC records (Fig 4b, c and e). This condition persisted until ca. 140 ka BP, when a
554 decline in spring/summer sea ice (PIPISO₂₅) is observed, accompanied by a rise in TOC and subsurface
555 ocean temperature (Fig. 4b, e and g). At a more northerly location in the South Scotia Sea, core
556 PS67/219-1 records a less pronounced sea-ice cover during the PGM with WSIC fluctuating at around
557 65% and a 1-3% abundance of *F. obliquecostata* suggesting the proximity of a permanent sea-ice edge
558 (Fig. 4d). These findings from the geological record are supported by our model simulation for the 140
559 ka BP time-slice, which shows an overall high simulated-WSI cover (94%; 92%), but slightly lower
560 simulated-spring/summer sea-ice cover (79%; 27%) at core sites PS118_63-1 and PS67/219-1,
561 respectively (Fig. 5a). Likewise, higher ssNa⁺ concentrations and $\delta^{18}\text{O}$ values from EDML ice core point
562 to cold conditions and an extensive sea-ice cover in the Atlantic region (Fig. 4a and j; EPICA Community
563 Members, 2006; Fischer et al., 2007).

564 Termination II (TII; 140-130 ka BP) marks the transition from a glacial into an interglacial
565 environment. The onset of this deglaciation was probably initiated by a warming event caused by a
566 maximum southern high latitude summer insolation at around 138 ka BP (Bianchi and Gersonde, 2002;
567 Broecker and Henderson, 1998) and further sustained by the Heinrich Stadial 11 (HS11) event
568 occurring in the Northern Hemisphere (NH) between 135 and 130 ka BP (Turney et al., 2020). The
569 HS11 is a prominent North Atlantic meltwater event that may have triggered the eventual shutdown of
570 the AMOC, thus reinforcing the warming in the SO via the bipolar seesaw effect (Marino et al., 2015).

571 In the Powell Basin, the WSIC remains high (100%) and only starts to decrease (80%) at ca. 134
572 ka BP, while gradually declining PIPSO₂₅ values since 140 ka BP accompany the onset of the
573 deglaciation and mark a shift from a perennial sea ice to a dynamic seasonal sea-ice cover (see Sect
574 4.5 for definition). A concurrent rise in subsurface ocean temperature is also observed during this
575 timeframe. In contrast, core PS67/219-1 in the South Scotia Sea recorded a different sea-ice regime
576 with generally lower and declining WSIC and <1% abundance of *F. obliquocostata*, suggesting a less
577 extended sea-ice cover. The different sea-ice conditions in both regions are supported by a higher
578 biogenic opal production recorded in the South Scotia Sea as compared to the minimum biogenic opal
579 content observed for the Powell Basin (Fig. 4e and f). The Powell Basin TOC profile is also different
580 from its opal counterpart, with the former peaking between 135-131 ka BP. We surmise that this peak
581 may relate to a preferential growth environment for non-siliceous marine organisms and/or increased
582 input of terrestrial organic matter during this interval.

583 The persistent warming was interrupted by a short period of spring/summer sea ice (PIPISO₂₅) re-
584 expansion and weakened decline in WSI towards the end of TII (ca. 132-130 ka BP; Fig 4b and c),
585 along with an increasing *Chaetoceros RS* abundance that peaks at ca. 131 ka BP (Fig. 3e). These
586 conditions coincide with the northward shift of the sea-ice edge at ODP Site 1094 around 129.5 ka BP
587 (Bianchi and Gersonde, 2002). A comparable reduction in SSST at around 131 ka BP is also observed
588 in the South Scotia Sea (core PS67/219-1, Fig. 4i) and apparent at ODP Site 1089 and core PS2821-1
589 (Cortese and Abelmann, 2002). In the Powell Basin, however, this cooling event is not reflected in
590 ocean temperature (Fig. 4g) and we propose that the lack of temperature change during this event may
591 be attributed to the discharge of meltwater from expanding sub-ice shelf cavities, which caused a
592 stronger stratification and an effective isolation of the warmer subsurface layer.

593 5.1.2 Last Interglacial - MIS 5 stadials/interstadials

594 Following the short-lived sea-ice expansion in Powell Basin at the end of TII, we observe a rapid
595 decline, and minimum spring/summer sea-ice cover is reached (see Sect 4.5) by ca. 129 ka BP (Fig.
596 4b). Lowest spring/summer sea ice (PIPISO₂₅) is observed between 126 and 124 ka BP, while minimum
597 WSIC is observed around 119 ka BP. These conditions promoted primary productivity, as reflected in
598 the maximum biogenic opal and TOC contents, at the respective timeframes (Fig. 4e). Likewise, sea
599 ice and temperature profiles from core PS67/219-1, the EDML ice core and model simulations also
600 favor a warm and predominantly open ocean condition for the South Atlantic sector throughout the LIG
601 (Fig. 4d, 4i, 5.3 and 6.3; EPICA Community Members, 2006; Fischer et al., 2007). Holloway et al.
602 (2017) investigated the simulated-spatial structure of the Antarctic WSI minimum at 128 ka BP with

603 respect to the $\delta^{18}\text{O}$ -isotopic peak recorded in the East Antarctic ice cores. They tested numerous WSI
604 retreat scenarios and concluded that the $\delta^{18}\text{O}$ maximum could be explained by a significant decline in
605 Antarctic WSI, with the Atlantic sector experiencing the largest reduction of 67%. Contrastingly, while
606 our spring/summer sea ice (PIPSO₂₅) data aligns with their $\delta^{18}\text{O}$ -accorded simulated-findings, our
607 diatom data - revealing a constant presence of WSI in the Powell Basin and South Scotia Sea with even
608 minor increases between 130 and 127 ka BP - disagrees. Furthermore, the WSI record from marine
609 core PS2305-6, located slightly north of our core site, also indicates the presence of WSI during MIS
610 5e (see also Supplementary Table S1 in Holloway et al., 2017; Bianchi and Gersonde, 2002; Gersonde
611 and Zielinski, 2000). We assume that the modeled winter sea-ice retreat seems to be valid for more
612 distal ocean areas, whereas at the core sites in Powell Basin and South Scotia Sea, ice-sheet-derived
613 meltwater may have acted as a driving mechanism fostering local sea-ice formation during winter, which
614 is not captured by the simulation in Holloway et al. (2017). Interestingly, the herein simulated sea ice at
615 the 128 ka BP time-slice corroborates our proxy-based data, indicating the presence of WSI in the
616 region amidst lower sea-ice concentration and continued retreat of sea ice over the spring/summer
617 seasons (Fig. 5.2). A similar sea-ice scenario is also established for the 125 ka BP time-slice,
618 considered to be the warmest period of the LIG (Fig. 5.3; Goelzer et al., 2016; Hoffman et al., 2017),
619 where Southern Hemisphere (SH) mid- to high-latitude spring insolation forcing reached a maximum
620 within the period from 130 ka BP to 125 ka BP (Lunt et al., 2013). The contrasting observation between
621 our marine sediment proxy and model data against that of the ice core $\delta^{18}\text{O}$ -accorded simulated-finding
622 emphasizes the need for more robust marine-based reconstructions, especially south of the modern
623 sea-ice edge, to sufficiently substantiate model results for these regions, and to enable comprehensive
624 input knowledge for future model simulations and predictions (Holloway et al., 2017; Otto-Bliesner et
625 al., 2013).

626 The reconstructed SSST trends in the Powell Basin and the South Scotia Sea are largely
627 comparable with the atmospheric temperature profile from the EDML ice core (Fig. 4h-j), suggesting
628 atmosphere-ocean interactions in the study area. The lack of significant glacial-interglacial temperature
629 variability within the Powell Basin could potentially be linked to its locality and close proximity to the
630 continental margin, where constant mixing of cold ice-shelf water with the WDW persists. Within the
631 Powell Basin, both the SSST and subsurface ocean temperature started to decrease around 130 ka
632 BP. While the SSST appeared to have cooled from -0.2°C to -0.4°C (127 ka BP) and recovered
633 thereafter – similar to the dip observed in the EDML $\delta^{18}\text{O}$ profile – the subsurface ocean temperature
634 declined distinctly from 0 to ca. -1.9°C and remained cold until 124 ka BP (Fig. 4g and h). The variance
635 in the magnitude of decline observed between the two temperature records (SSST vs. OT) may be
636 attributed to the distinctly different seasonal signals depicted by the proxies (i.e., summer vs. annual
637 temperature) and water depths (0-10 m vs. 0-200 m; see also Sect 4.2 and 4.3). We speculate that the
638 decline in seawater temperature since 130 ka BP may be the result of intense melting of the Antarctic
639 ice sheet and sea ice, leading to a freshening of coastal waters. Similar to the modern-day Weddell
640 Gyre circulation (see Sect 2 for details), the increased discharge of cold (sea) ice-shelf meltwater into
641 the Powell Basin, via the Antarctic Coastal Current and Antarctic Slope Current, may have deepened
642 the cold-water stratification in the basin, thus causing the observed dip in ocean temperature between

643 130 and 124 ka BP. Turney et al. (2020) discovered that the WAIS had retreated from the Patriot Hills
644 blue ice area by the end of TII (130.1 ± 1.8 ka BP). This area is located 50 km inland from the present-
645 day grounding line of the Filchner-Ronne Ice Shelf. Their investigation revealed a 50 kyrs hiatus in the
646 blue ice record, indicative of a collapse of the ice shelf at the end of TII, followed by its subsequent
647 recovery during late MIS 5. Holloway et al. (2016) also propose a maximum ice-sheet retreat at around
648 126 ka BP based on distinct differences between the isotopic records observed for Mt Moulton and East
649 Antarctic ice cores. Assuming that the distinct reduction in spring/summer sea-ice recorded in core
650 PS118_63-1 was not confined to the Powell Basin but may reflect a more extensive sea ice decline in
651 the Weddell Sea embayment, we posit that this loss of sea ice (i.e., the loss of an effective buffer
652 protecting ice-shelf fronts) may have accelerated the disintegration of the Weddell Sea ice shelves and,
653 ultimately, the WAIS.

654 Following the peak of the LIG around 119 ka BP, the Powell Basin sea-ice records reflect a cycle
655 of sea ice advance and retreat throughout the remaining MIS 5 substages. WSIC strengthened and
656 remained at ca. 80%, while spring/summer sea ice (PIP_{SO25}) experienced a substantial increase
657 between MIS 5e and 5d (reaching PGM values at 5d), and remained elevated (> ca. 0.6) for the rest of
658 the MIS (Fig. 4b and c). This expansion of sea ice into MIS 5d, and its persisting presence throughout
659 the remaining MIS 5, is accompanied by a gradual decline in both sea surface and subsurface ocean
660 temperatures, along with reduced primary production. Likewise, an increasing WSIC, lowered SSST
661 and primary productivity are also noted in the South Scotia Sea (Fig. 4d-h). However, being more
662 northerly located, the South Scotia Sea experienced a lower and more varied WSIC (ca. 48 - 68%)
663 and minimum summer sea-ice cover evident by a lower abundance of *F. obliquecostata* (<1%) than in
664 the Powell Basin (Fig. 4d).

665 5.1.3 Glacial period – Last Glacial Maximum – Termination I

666 After MIS 5, Antarctica transited into the last glacial period (74-19 ka BP). In our Powell Basin
667 records, this is reflected in a northward expansion of the sea-ice extent (peak PIP_{SO25} values and 100%
668 WSIC). Additionally, the lack of sea ice- and phytoplankton-related biomarkers and diatoms points
669 towards an extremely suppressed production in the basin (Fig. 3a and b, 4b and c). We postulate that
670 at that time the basin was likely covered by permanent sea-ice cover or a floating ice shelf, which
671 inhibited primary production in the underlying water column. The South Scotia Sea record (PS67/219-
672 1) further to the north also points to an overall higher winter and summer sea-ice cover, with elevated
673 abundance of *F. obliquecostata* (0 - 3%) during this period suggesting a permanent sea-ice edge close
674 to the core site (Xiao et al., 2016a). The oscillating patterns observed in both the sea-ice record and the
675 biogenic opal content further point to alternating advance and retreat phases of the sea-ice edge in the
676 South Scotia Sea (Fig. 4d and f; Allen et al., 2011).

677 In the Powell Basin, capped by an overlying (sea) ice cover throughout the glacial period,
678 subsurface ocean temperatures somewhat resemble the millennial-scale variability in the EDML
679 temperature profile (Fig. 4g). We presume that the subsurface temperature variations may possibly
680 reflect changes in the ocean circulation in the Atlantic sector of the SO (Böhm et al., 2015; Williams et
681 al., 2021). However, the age uncertainties and the low resolution of our subsurface ocean temperature

682 record hamper an affirmative conclusion, and more data points will be required to ascertain
683 corresponding oceanic variability.

684 The last glacial period culminated during the LGM between 26.5 and 19 ka BP with a most
685 northwardly extending sea-ice edge, as identified in several marine sediment cores (Fig. 4b and c;
686 Gersonde et al., 2005; Xiao et al., 2016a) and deduced from maximum ssNa⁺ concentrations in the
687 EDML ice core (Fig. 4a; Fischer et al., 2007). Evidence from previous studies indicated the advance of
688 grounded ice sheet and island ice caps to the edge of the outer continental shelf (Davies et al., 2012;
689 Dickens et al., 2014). These grounded ice sheets were surrounded by floating ice shelves that extended
690 seaward to 58°S on the western side of Antarctica (Herron and Anderson, 1990; Johnson and Andrews,
691 1986). In the Atlantic sector, the 60 - 70% expansion of WSI towards the modern Polar Front (~50°S;
692 Gersonde et al., 2003) also promoted a northward shift of the summer sea-ice edge beyond core site
693 PS67/219-1 to around 55°S (Allen et al., 2011; Collins et al., 2012), which lead to restricted primary
694 productivity as reflected in the minimum biogenic opal content of core PS67/219-1 (Fig. 4f). The LGM
695 is also considered the coldest interval, with a northward expansion of the (sub)Antarctic cold waters by
696 4 - 5° in latitude towards the subtropical warm waters (Gersonde and Zielinski, 2000; Gersonde et al.,
697 2003). Sea-ice extent (Fig. 5.4) and SSST (Fig. 6.3) derived from our climate simulation during the peak
698 of LGM (21 ka BP) align with these findings. This distinct growth of the (sea) ice-field in the SO, coupled
699 with lower reconstructed and modeled LGM subsurface temperatures (Fig. 4g and 7.3), suggests an
700 intensified cold-water stratification at our core sites, and a possible northward displacement of the WDW
701 upwelling zone towards the edge of the summer sea-ice field (Ferrari et al., 2014).

702 TI began around 18 ka BP, when our records from Powell Basin indicate a transition from a
703 perennial-ice cover to a dynamic sea-ice scenario (see Sect 4.5), with several cycles of advance and
704 retreat. Similarly, the sea ice-related records from the South Scotia Sea (PS67/219-1) and the EDML
705 ssNa⁺ record depict a decrease in sea-ice cover, along with rapid increases in primary productivity and
706 ocean temperature (Fig. 4). This deglaciation is attributed to a weakening AMOC circulation as a result
707 of reduced NADW formation caused by increasing NH summer insolation and significant ice sheet melt
708 at 18 ka BP, also known as Heinrich Stadial 1 (Clark et al., 2020; Denton et al., 2010; Waelbroeck et
709 al., 2011). The gradual warming of TI was interrupted by a brief cooling between 14 and 12 ka BP.
710 During this interval, our records reveal a short-term re-advancement in sea ice, coupled with a drop in
711 productivity and temperature (Fig. 4). This event seems to coincide with multiple South Atlantic records
712 (Xiao et al., 2016a) and higher ssNa⁺ concentrations and a plateau in $\delta^{18}\text{O}$ values recorded in the EDML
713 ice core (Fischer et al., 2007). We hence propose this event to be the Antarctic Cold Reversal (ACR),
714 which is linked to the Bølling-Allerød warm interval in the NH via the bipolar seesaw mechanism (Pedro
715 et al., 2011; 2016).

716 5.1.4 *Holocene*

717 Following the brief cooling of the ACR, the deglacial warming resumed its pace and Antarctica
718 transited into the present interglacial (Holocene: 12 ka BP-present), which is marked by intervals of
719 warming and cooling events (Bentley et al., 2009; Bianchi and Gersonde, 2004; Xiao et al., 2016a). Our
720 data support these findings and document periods characterized by seasonal/dynamic and minimum

721 sea-ice cover (see Sect 4.5) since 12 ka BP. We acknowledge that the age constraints and data
722 availability of core PS118_63-1 for the Holocene is limited and exercise caution on the interpretation of
723 the Holocene proxy records. Nevertheless, our data still permit the discrimination of Holocene warming
724 and cooling trends.

725 The Powell Basin experienced an overall rapid decline in the winter and spring/summer sea-ice
726 (Fig. 4b and c), concurrent with a rise in SSST (-0.5 to 0.5°C; Fig. 4h) and primary productivity between
727 12 and 5 ka BP (Fig. 4e), suggesting a seasonal sea-ice cover. The significant reduction in the
728 abundance of the *F. curta* gp (below 3%), WSIC and spring/summer sea ice (PIPSO₂₅; Fig. 4b and c)
729 culminates at ca. 5 ka BP and is accompanied by an elevated primary productivity reflected in rising
730 biogenic opal and TOC contents, which seems to indicate a brief open-ocean setting for the Powell
731 Basin during this warm interval. We further note fluctuating SSSTs, while the subsurface ocean
732 temperature remains relatively stable between 9 and 5 ka BP and the remainder of the Holocene (Fig.
733 4g and h). This somehow contrasts with a subtle decline in SSSTs recorded in core PS67/219-1 (Fig.
734 4i) in the South Scotia Sea, substantiated by the elevated presence of *Chaetoceros* rs recorded in core
735 PS118_63-1 (Fig. 3e). We may attribute this cooling to a northward export of increased glacial
736 meltwater. Our model simulation at 6 ka BP depicts a somewhat similar oceanic condition, with <40%
737 spring/summer sea ice at the studied sites (Fig. 5.5a). However, in comparison with our proxy records,
738 the model appears to have overestimated the WSI, SST and OT (Fig. 5.5b, 6.4 and 7.4). This
739 overestimation may be attributed to the complex ice-ocean interactions and feedbacks along the
740 Antarctic coastal region, which may not be fully represented in the model that has a spatial resolution
741 in the order of tens of kilometers.

742 While the limited age constraints for the Holocene in core PS118_63-1, preclude us from further
743 allocating short-term climate variations, we propose that the interval around 5 ka BP may reflect the
744 Holocene climate optimum, while the upper part of the core depicts the later Holocene conditions. Here,
745 increasing PIPSO₂₅ values and WSI reflect a re-expansion of seasonal sea ice still permitting primary
746 productivity as derived from elevated biogenic opal and TOC contents (Fig. 4b, c and e). The climate
747 optimum experienced in the Powell Basin seems to correspond to the mid-Holocene climate optimum
748 identified in sediment cores from the South Orkney Plateau between 8.2 and 4.8 ka BP and around
749 Antarctica (Crosta et al., 2008; Denis et al., 2010; Kim et al., 2012; Lee et al., 2010; Taylor et al., 2001).
750 However, reports of differing timings and mode for the mid-Holocene climate optimum around the
751 Antarctic Peninsula have been noted in previous studies (Bentley et al., 2009; Davies et al., 2012;
752 Shevenell et al., 1996; Taylor and Sjunneskog, 2002). Vorrath et al. (2023) determined the mid-
753 Holocene climate optimum to have occurred between 8.2 and 4.2 ka BP, based on biomarker analyses
754 of a sediment core from the eastern Bransfield Strait. They suggest that the climatic changes at their
755 core site were influenced predominantly by the warm Antarctic Circumpolar Current rather than the
756 cold-water Weddell Sea. This is contrary to a shorter climate optimum (6.8-5.9 ka BP) proposed by
757 Heroy et al. (2008), where they examined the climate history of western Bransfield Strait using sediment
758 and diatom analyses. Such diverse research outcomes highlight the complexity of responses to micro-
759 region variations in glacial, atmospheric and oceanic changes in the Antarctic Peninsula throughout the
760 Holocene (Bentley et al., 2009; Davies et al., 2012; Heroy et al., 2008; Vorrath et al., 2023).

761 5.2 Comparison between interglacials / transition periods

762 A comparison of the environmental changes caused by climate warming during TII and TI as well
763 as the peak LIG and the Holocene, may yield valuable information on common or different driving and
764 feedback mechanisms. As marine cores PS118_63-1 and PS67/219-1 provide continuous records of
765 the environmental evolution in the northwestern Weddell Sea and South Scotia Sea, respectively, dating
766 back to at least 145 ka BP, they offer a distinct opportunity to evaluate (sea-ice) conditions between the
767 two terminations (TII and TI) and both warm periods (LIG and Holocene), particularly in proximity to the
768 continental margin. Denton et al. (2010) studied the last four terminations and concluded that the
769 terminations were triggered by a sequence of comparable events: maximum NH summer insolation that
770 caused substantial NH ice sheet melting (due to marine ice sheet instability) over an extended (>5 kyrs)
771 NH stadial interval. The huge release of meltwater slowed the AMOC, thus triggering an intense
772 warming in the southern high-latitudes through the bipolar seesaw teleconnection, accompanied by a
773 poleward shift in the southern westerlies. In line with this hypothesis, our records from cores PS118_63-
774 1 and PS67/219-1 portray a consistent and rapid decline in sea ice throughout both terminations (TII
775 and TI). Interestingly, both deglaciations feature a short-term readvance of sea ice during their latest
776 stage, at ca. 130 ka BP and during the ACR, respectively, likely due to meltwater-discharge from
777 retreating ice shelves/ice sheets in the SO. This suggests that short-term sea ice growth stimulated by
778 deglacial meltwater may be a common feature during glacial terminations. Despite commonalities in the
779 sea-ice records, some differences are discernible. For instance, during TII, there is an abrupt surge in
780 biogenic opal in the South Scotia Sea, along a consistent rise in TOC content within the Powell Basin.
781 In contrast, TI exhibits a pattern characterized by a gradual increase with periodic fluctuations
782 throughout the termination for both TOC and biogenic opal content. Additionally, the South Scotia Sea
783 (PS67/219-1) recorded a higher mean biogenic opal content and SSST across TII (35%; 0.7°C) than TI
784 (26%; 0.5°C). Likewise, in the Powell Basin (PS118_63-1), higher mean TOC and subsurface ocean
785 temperature are perceived during TII (0.5%; 0°C) than during TI (0.4%; -0.3°C). These data are in
786 agreement with the EDML $\delta^{18}\text{O}$ record, which registered a stronger deglacial amplitude (32%) in TII
787 than TI (Masson-Delmotte et al., 2011). Broecker and Henderson (1998) also speculated that the
788 amplitude of the SH summer insolation during TII was higher than during TI. Additionally, a delay of
789 approximately 10 kyrs between the SH and NH summer insolation (and subsequent NH ice sheet
790 melting) during TII – as compared to TI's SH summer insolation peak just before the melting of the NH
791 ice sheet – probably contributed to a more pronounced TII warming in the SO. The differing magnitude
792 of warming observed between both core sites in the South Atlantic, however, is likely attributed to their
793 latitudinal differences.

794 The climate during the LIG appeared to be warmer than during the Holocene. In the Powell Basin,
795 the LIG peak interval (i.e., MIS 5e) was characterized by a significantly reduced spring/summer sea-ice
796 cover and peak productivity, while a higher spring/summer sea-ice cover, along with an only gradually
797 increasing productivity are observed for the Holocene warm period (Fig. 4b and e). However, no
798 significant difference in the WSIC between both interglacial was noted. The discrepancy in warming
799 intensity likely occurred seasonally and coincided with maximum summer insolation (see also Fig. 4 in
800 Bova et al., 2021). Nonetheless, a lower mean annual regional insolation (-1.1 W/m² difference; Laskar

801 et al., 2004) during the LIG does not explain the warmer conditions observed in the region. Bova et al.
802 (2021) hypothesized that the LIG was relatively warmer than the Holocene as a result of its preceding
803 deglacial dynamics: specifically, the magnitude of the last deglaciation was half that of the penultimate
804 deglaciation – where a rapid and intense warming destabilized and significantly reduced the (sea) ice
805 cover to near modern-day level by the onset of the LIG (Bova et al., 2021), and possibly a collapse of
806 the WAIS in the first half of the LIG (Pollard and Deconto, 2009; Sutter et al., 2016). As such, we opine
807 that the lower magnitude of warming during TI was a consequence of spatially and temporally varying
808 retreats and advances in ice cover (including sea ice, ice shelves and glaciers) in the SO. The higher
809 ice coverage throughout the Holocene resulted in a higher surface albedo and a cooler Holocene, as
810 compared to the LIG. This is witnessed in our rather variable Holocene sea-ice proxy records (Fig. 4b
811 and c) and differing reports of mid-Holocene warming and repeated fluctuations in environmental
812 conditions around Antarctica (see sect 5.1.4; Bentley et al., 2014; Davies et al., 2012; Ó Cofaigh et al.,
813 2014).

814 **5.3 Evaluating COSMOS performance: Addressing boundary conditions and model selection**

815 With regard to COSMOS simulations, we note very similar sea-ice conditions being depicted for
816 the peak interglacial 125 ka BP and 6 ka BP time slices (Fig 5.3 and 5.5), while subtle differences are
817 resolved for SSTs and OTs (Fig. 6.2 and 6.4, 7.2 and 7.4, respectively). When considering the disparity
818 observed in our proxy data between these two interglacial intervals, we infer that these similarities in
819 the simulations likely result from using the same geographic boundary conditions for both time slices,
820 while climate forcing data (e.g., greenhouse gases, orbital parameters) differ, of course. Our study
821 aligns with the PMIP framework in maintaining a constant modern-day geography across each
822 interglacial time slice, specifically the mid-Holocene (e.g., 6 ka BP) and the LIG (e.g., 128 and 125 ka
823 BP). For the 6 ka BP time slice, this decision is supported by evidence indicating that ice sheets had
824 reached their modern configuration (Otto-Bliesner et al., 2017). In the case of the LIG, the use of the
825 modern ice-sheet configuration is primarily due to uncertainties in the LIG reconstructions (Otto-Bliesner
826 et al., 2017). We acknowledge that the consideration of a single configuration throughout the LIG
827 certainly is a simplification. However, it is also important to note that the changes in the Antarctic ice
828 sheets' contribution to global mean sea level were small between 128 and 125 ka BP, compared to the
829 remainder of the LIG (Barnett et al., 2023). Therefore, we propose that using a constant ice-sheet
830 configuration for our LIG time slices is a reasonable approximation. Similarly, we estimated a constant
831 ice-sheet setting for both the PGM and LGM time slices. While there are indications of different NH ice-
832 sheet extents between the two glacial periods (Rohling et al., 2017), uncertainty remains regarding the
833 exact distribution of ice on Antarctica. Understanding this distribution is crucial to determine whether
834 different ice-sheet configurations should be considered for the boundary conditions of the respective
835 glacial climate simulations. Given the varied trends observed in our proxy data for each glacial and
836 interglacial periods, we propose that future studies should explore different plausible Antarctic ice-sheet
837 configurations and their effects on glacial-interglacial sea ice and oceanic conditions in the SO,
838 particularly in the coastal regions.

839 In our modeling approach, we have relied exclusively on simulations from COSMOS rather than
840 adopting a multi-model approach based on available PMIP simulations. This decision was motivated by
841 the need to cover specific time slices pertinent to our study (see also Sect 3.5). To validate the reliability
842 of our results, we conducted a comparison of COSMOS-simulated sea-ice cover and SST results
843 against those from the PMIP3 and PMIP4 ensemble models. We refer to Supplement S3.4 for full detail.
844 In general, the model-to-model comparison shows good agreement ($<2\sigma$ threshold) between our
845 COSMOS results and those from the PMIP3 ensemble – especially at our study locations, with some
846 disagreement noted for the 21 ka BP time slice (Supplementary Fig. S4 and S5, S8 and S9). These
847 deviations largely occur around the sea-ice edge and are primarily due to uncertainties generated within
848 the PMIP3 ensemble itself. In contrast, our COSMOS-to-PMIP4 ensemble comparison shows greater
849 disagreement. The COSMOS simulation shows a milder warm bias in the SO compared to various other
850 PMIP3 models (Lunt et al., 2013), whereas CMIP6 models, which provide the foundation for PMIP4,
851 are documented to have a warm bias in the SO (Luo et al., 2023). Beyond the difference in warm bias,
852 the disagreements between COSMOS and PMIP4 may arise from several factors, including evolution
853 of modeling protocols, boundary conditions, and model development from PMIP3 to PMIP4, with
854 COSMOS remaining a PMIP3-class model. Based on the comparative outcomes, we demonstrate that
855 our results align with PMIP in many relevant aspects, though this comparison is limited by the
856 incomplete coverage of time slices within PMIP. Where our model shows disagreement with the PMIP3
857 ensemble, the uncertainty within the ensemble itself is quite large. This highlights that the uncertainty
858 in simulated sea-ice conditions at our core locations, which we acknowledge as a limitation of using
859 only one model in our study, is not necessarily mitigated by using an ensemble of models instead. Given
860 that COSMOS is mostly within the 2σ threshold – defined as a measure for agreement with the PMIP3
861 ensemble – at the study sites, we would not expect to derive substantially different inferences if we
862 relied on the PMIP3 ensemble instead. Although COSMOS has not undergone the updates that PMIP4
863 models received and has been exposed to boundary conditions only partly comparable to PMIP4
864 simulations, it remains one of the most extensively utilized models for reconstructing Quaternary
865 climates and beyond to date. This enables our study’s results to be considered within the much larger
866 context of the Cenozoic climate. Despite these limitations, it is worth noting that COSMOS has been
867 successfully employed alongside other PMIP4 models (Stepanek et al., 2020).

868 **6 Summary and conclusions**

869 Multiproxy analyses on marine sediment core PS118_63-1 from the Powell Basin provide new
870 insights into the glacial-interglacial environmental variability in proximity to the Antarctic continental
871 margin. With the use of the novel sea ice and open-water biomarkers and diatom assemblage data,
872 alongside primary productivity proxies, we are able to reconstruct sea-ice conditions in the Powell Basin
873 for the past ca. 145 kyrs. Our findings reveal year-round ice-cover with minimal productivity during
874 glacial periods, while dynamic sea-ice conditions with varied productivity are recorded in the Powell
875 Basin during climate transitions and interglacial periods, such as the Holocene and MIS 5. Peak
876 reduction in sea ice and near open ocean conditions are noted for MIS 5e. In contrast, no significant

877 glacial-interglacial temperature variation was registered in the basin, which is attributed to the cold-
878 water regime of the Weddell Sea. Comparison between the current and last interglacial, and their
879 respective climate transitions (TI and TII), suggests a relationship between deglacial amplitude and
880 warming intensity during the corresponding interglacial: in general, an abrupt and intense (gradual and
881 slow) deglaciation leads to a warmer (cooler) interglacial, with higher (lesser) ice-sheet retreat (Bova et
882 al., 2021). Our data presented in this study reinforce earlier paleo sea-ice reconstructions in the South
883 Atlantic sector of the SO and provide new insights into the ice-proximal sea-ice response during varying
884 climate conditions. Evaluation of both proxy and model data highlights similarities between sea-ice
885 reconstruction and simulation. However, notable discrepancies remain, such as the differing proxy-
886 model data observed for the Holocene compared to the LIG, and subsurface temperature profile for the
887 LIG. It is therefore pivotal to explore different Antarctic ice-sheet configurations in future studies, as well
888 to expand on the paleoclimate data for the region. These will help to close the gap in our understanding
889 of ocean-ice-atmosphere interactions and dynamics and ultimately enhance climate model predictions
890 closer to the Antarctic continental margins.

891

892 **Data availability.** Data mentioned in this article will be available on PANGAEA (Proxy records: address;
893 COSMOS model output: address). For specific model output requests beyond the climate variables
894 included in the PANGAEA data publication, please contact Christian Stepanek at
895 christian.stepanek@awi.de. CMIP/PMIP data is available via the Earth System Grid Federation using
896 one of their publicly available data portals (e.g., [https://esgf-data.dkrz.de/search/cmip5-](https://esgf-data.dkrz.de/search/cmip5-dkrz/)
897 [dkrz/](https://esgf-data.dkrz.de/search/cmip5-dkrz/) and [https://esgf-data.dkrz.de/search/cmip6-](https://esgf-data.dkrz.de/search/cmip6-dkrz/)
898 [dkrz/](https://esgf-data.dkrz.de/search/cmip6-dkrz/)).

898

899 **Code availability.** Requests for the source code of the COSMOS climate model should be directed to
900 the Max Planck Institute for Meteorology, Bundesstrasse 53, 20146 Hamburg, Germany.

901

902 **Supplement.** The supplement related to this article is available online at:

903

904 **Author contributions.** This study was conceived by WWK and JM. Data collection and interpretation
905 was conducted by WWK, together with OE (diatom), JM (HBI), JH and GM (GDGT). WG produced the
906 U/Th-dating data. CS and GL selected, documented, and post-processed the data from an ensemble
907 of simulations that provided the climate model data for this study. Three of the six simulations presented
908 here, namely *lig125k*, *lig128k*, and *pgm140k*, represent previously unpublished climate model output
909 created by PG. WX supplied unpublished data for PS67/219-1. WWK wrote the paper and created the
910 visualizations, supported by CS who visualized model output and interpolated climate model output to
911 core locations. JM supervised the study. All authors contributed to the analyses, discussion of the
912 results, and the conclusion of this study.

913

914 **Competing interests.** The authors declare that they have no conflict of interest.

915

916 **Acknowledgements.** We thank the captain, crew and science team of the RV Polarstern cruise PS118
917 (Grant No. AWI_PS118_04). Special thanks go to Michael Schreck, Nele Steinberg, Sabine Hanisch
918 and Frank Niessen for PS118 marine geology operations. Appreciation is also extended to Denise
919 Diekstatt (HBI), Mandy Kuck (HBI), Ulrike Böttjer (Biogenic Opal) for their support. Simon Belt is
920 acknowledged for providing the 7-HND internal standard for HBI quantification. This research is funded
921 through the Alfred Wegener Institute Helmholtz Centre for Polar and Marine Research (International
922 Science Program for Integrative Research in Earth Systems, INSPIRES II). Gerrit Lohmann, Paul Gierz,
923 and Christian Stepanek are funded through the Alfred Wegener Institute's research program: Changing
924 Earth - Sustaining our Future of the Helmholtz Association. Christian Stepanek also acknowledges
925 funding from the Helmholtz Climate Initiative REKLIM. We acknowledge the World Climate Research
926 Programme's Working Group on Coupled Modeling for CMIP, and the Paleoclimate Model
927 Intercomparison Project and its working groups for coordinating the model intercomparison in PMIP3
928 and PMIP4. Appreciation is extended to the climate modeling groups (listed in Table S4) for their
929 contribution and availability of model output to CMIP5/6 and PMIP3/4. The U.S. Department of Energy's
930 Program for Climate Model Diagnosis and Intercomparison is recognized for providing coordinating
931 support and leading software infrastructure development with the Global Organization for Earth System
932 Science Portals. The Earth System Grid Federation is also acknowledged for preserving and providing
933 CMIP and PMIP model output. We are also appreciative of the support from the Alfred Wegener
934 Institute's Open Access Publication Funds. Lastly, we thank the editor, Dr. Alberto Reyes, Dr. Xavier
935 Crosta and an anonymous reviewer for their constructive comments that helped to improve the paper.

936 **References**

- 937 Abe-Ouchi, A., Saito, F., Kageyama, M., Braconnot, P., Harrison, S. P., Lambeck, K., Otto-Bliesner, B.
938 L., Peltier, W. R., Tarasov, L., Peterschmitt, J. Y., and Takahashi, K.: Ice-sheet configuration in the
939 CMIP5/PMIP3 Last Glacial Maximum experiments, *Geosci. Model Dev.*, 8, 3621-3637,
940 <https://doi.org/10.5194/gmd-8-3621-2015>, 2015.
- 941 Abernathy, R. P., Cerovecki, I., Holland, P. R., Newsom, E., Mazloff, M., and Talley, L. D.: Water-mass
942 transformation by sea ice in the upper branch of the Southern Ocean overturning, *Nature Geoscience*,
943 9, 596-601, <https://doi.org/10.1038/ngeo2749>, 2016.
- 944 Abram, N. J., Wolff, E. W., and Curran, M. A. J.: A review of sea ice proxy information from polar ice
945 cores, *Quaternary Science Reviews*, 79, 168-183, <https://doi.org/10.1016/j.quascirev.2013.01.011>,
946 2013.
- 947 Allen, C. S., Pike, J., and Pudsey, C. J.: Last glacial–interglacial sea-ice cover in the SW Atlantic and
948 its potential role in global deglaciation, *Quaternary Science Reviews*, 30, 2446-2458,
949 <https://doi.org/10.1016/j.quascirev.2011.04.002>, 2011.
- 950 Argus, D. F. and Peltier, W. R.: Constraining models of postglacial rebound using space geodesy: a
951 detailed assessment of model ICE-5G (VM2) and its relatives, *Geophysical Journal International*, 181,
952 697-723, <https://doi.org/10.1111/j.1365-246X.2010.04562.x>, 2010.
- 953 Bakker, P., Masson-Delmotte, V., Martrat, B., Charbit, S., Renssen, H., Gröger, M., Krebs-Kanzow, U.,
954 Lohmann, G., Lunt, D. J., Pfeiffer, M., Phipps, S. J., Prange, M., Ritz, S. P., Schulz, M., Stenni, B.,
955 Stone, E. J., and Varma, V.: Temperature trends during the Present and Last Interglacial periods – a

- 956 multi-model-data comparison, *Quaternary Science Reviews*, 99, 224-243,
957 <https://doi.org/10.1016/j.quascirev.2014.06.031>, 2014.
- 958 Barbara, L., Crosta, X., Schmidt, S., and Massé, G.: Diatoms and biomarkers evidence for major
959 changes in sea ice conditions prior the instrumental period in Antarctic Peninsula, *Quaternary Science*
960 *Reviews*, 79, 99-110, <https://doi.org/10.1016/j.quascirev.2013.07.021>, 2013.
- 961 Barbara, L., Crosta, X., Leventer, A., Schmidt, S., Etourneau, J., Domack, E., and Massé, G.:
962 Environmental responses of the Northeast Antarctic Peninsula to the Holocene climate variability,
963 *Paleoceanography*, 31, 131-147, <https://doi.org/10.1002/2015PA002785>, 2016.
- 964 Barnett, R. L., Austermann, J., Dyer, B., Telfer, M. W., Barlow, N. L. M., Boulton, S. J., Carr, A. S., and
965 Creel, R. C.: Constraining the contribution of the Antarctic Ice Sheet to Last Interglacial sea level,
966 *Science Advances*, 9, eadf0198, <https://doi.org/10.1126/sciadv.adf0198>, 2023.
- 967 Belt, S. T.: Source-specific biomarkers as proxies for Arctic and Antarctic sea ice, *Organic*
968 *Geochemistry*, 125, 277-298, <https://doi.org/10.1016/j.orggeochem.2018.10.002>, 2018.
- 969 Belt, S. T. and Müller, J.: The Arctic sea ice biomarker IP25: a review of current understanding,
970 recommendations for future research and applications in palaeo sea ice reconstructions, *Quaternary*
971 *Science Reviews*, 79, 9-25, <https://doi.org/10.1016/j.quascirev.2012.12.001>, 2013.
- 972 Belt, S. T., Allard, W. G., Massé, G., Robert, J.-M., and Rowland, S. J.: Highly branched isoprenoids
973 (HBIs): identification of the most common and abundant sedimentary isomers, *Geochimica et*
974 *Cosmochimica Acta*, 64, 3839-3851, [https://doi.org/10.1016/S0016-7037\(00\)00464-6](https://doi.org/10.1016/S0016-7037(00)00464-6), 2000.
- 975 Belt, S. T., Brown, T. A., Rodriguez, A. N., Sanz, P. C., Tonkin, A., and Ingle, R.: A reproducible method
976 for the extraction, identification and quantification of the Arctic sea ice proxy IP25 from marine
977 sediments, *Analytical Methods*, 4, 705-713, <https://doi.org/10.1039/C2AY05728J>, 2012.
- 978 Belt, S. T., Smik, L., Brown, T. A., Kim, J. H., Rowland, S. J., Allen, C. S., Gal, J. K., Shin, K. H., Lee,
979 J. I., and Taylor, K. W. R.: Source identification and distribution reveals the potential of the geochemical
980 Antarctic sea ice proxy IPSO25, *Nature Communications*, 7, 12655,
981 <https://doi.org/10.1038/ncomms12655>, 2016.
- 982 Bentley, M. J., Hodgson, D. A., Smith, J. A., Cofaigh, C. Ó., Domack, E. W., Larter, R. D., Roberts, S.
983 J., Brachfeld, S., Leventer, A., Hjort, C., Hillenbrand, C.-D., and Evans, J.: Mechanisms of Holocene
984 palaeoenvironmental change in the Antarctic Peninsula region, *The Holocene*, 19, 51-69,
985 <https://doi.org/10.1177/0959683608096603>, 2009.
- 986 Bentley, M. J., Ó Cofaigh, C., Anderson, J. B., Conway, H., Davies, B., Graham, A. G. C., Hillenbrand,
987 C.-D., Hodgson, D. A., Jamieson, S. S. R., Larter, R. D., Mackintosh, A., Smith, J. A., Verleyen, E.,
988 Ackert, R. P., Bart, P. J., Berg, S., Brunstein, D., Canals, M., Colhoun, E. A., Crosta, X., Dickens, W.
989 A., Domack, E., Dowdeswell, J. A., Dunbar, R., Ehrmann, W., Evans, J., Favier, V., Fink, D., Fogwill,
990 C. J., Glasser, N. F., Gohl, K., Golledge, N. R., Goodwin, I., Gore, D. B., Greenwood, S. L., Hall, B. L.,
991 Hall, K., Hedding, D. W., Hein, A. S., Hocking, E. P., Jakobsson, M., Johnson, J. S., Jomelli, V., Jones,
992 R. S., Klages, J. P., Kristoffersen, Y., Kuhn, G., Leventer, A., Licht, K., Lilly, K., Lindow, J., Livingstone,
993 S. J., Massé, G., McGlone, M. S., McKay, R. M., Melles, M., Miura, H., Mulvaney, R., Nel, W., Nitsche,
994 F. O., O'Brien, P. E., Post, A. L., Roberts, S. J., Saunders, K. M., Selkirk, P. M., Simms, A. R., Spiegel,
995 C., Stollendorf, T. D., Sugden, D. E., van der Putten, N., van Ommen, T., Verfaillie, D., Vyverman, W.,
996 Wagner, B., White, D. A., Witus, A. E., and Zwart, D.: A community-based geological reconstruction
997 of Antarctic Ice Sheet deglaciation since the Last Glacial Maximum, *Quaternary Science Reviews*, 100,
998 1-9, <https://doi.org/10.1016/j.quascirev.2014.06.025>, 2014.
- 999 Bianchi, C. and Gersonde, R.: The Southern Ocean surface between Marine Isotope Stages 6 and 5d:
1000 Shape and timing of climate changes, *Palaeogeography, Palaeoclimatology, Palaeoecology*, 187, 151-
1001 177, [https://doi.org/10.1016/S0031-0182\(02\)00516-3](https://doi.org/10.1016/S0031-0182(02)00516-3), 2002.
- 1002 Bianchi, C. and Gersonde, R.: Climate evolution at the last deglaciation: the role of the Southern Ocean,
1003 *Earth and Planetary Science Letters*, 228, 407-424, <https://doi.org/10.1016/j.epsl.2004.10.003>, 2004.

- 1004 Böhm, E., Lippold, J., Gutjahr, M., Frank, M., Blaser, P., Antz, B., Fohlmeister, J., Frank, N., Andersen,
1005 M. B., and Deininger, M.: Strong and deep Atlantic meridional overturning circulation during the last
1006 glacial cycle, *Nature*, 517, 73-76, <https://doi.org/10.1038/nature14059>, 2015.
- 1007 Bova, S., Rosenthal, Y., Liu, Z., Godad, S. P., and Yan, M.: Seasonal origin of the thermal maxima at
1008 the Holocene and the last interglacial, *Nature*, 589, 548-553, <https://doi.org/10.1038/s41586-020-03155-x>, 2021.
- 1010 Braconnot, P., Harrison, S. P., Kageyama, M., Bartlein, P. J., Masson-Delmotte, V., Abe-Ouchi, A.,
1011 Otto-Bliesner, B., and Zhao, Y.: Evaluation of climate models using palaeoclimatic data, *Nature Climate*
1012 *Change*, 2, 417-424, <https://doi.org/10.1038/nclimate1456>, 2012.
- 1013 Broecker, W. S. and Henderson, G. M.: The sequence of events surrounding Termination II and their
1014 implications for the cause of glacial-interglacial CO₂ changes, *Paleoceanography*, 13, 352-364,
1015 <https://doi.org/10.1029/98PA00920>, 1998.
- 1016 Brovkin, V., Raddatz, T., Reick, C. H., Claussen, M., and Gayler, V.: Global biogeophysical interactions
1017 between forest and climate, *Geophysical Research Letters*, 36, <https://doi.org/10.1029/2009GL037543>,
1018 2009.
- 1019 Carmack, E. C. and Foster, T. D.: On the flow of water out of the Weddell Sea, *Deep Sea Research*
1020 *and Oceanographic Abstracts*, 22, 711-724, [https://doi.org/10.1016/0011-7471\(75\)90077-7](https://doi.org/10.1016/0011-7471(75)90077-7), 1975.
- 1021 Chadwick, M., Allen, C. S., Sime, L. C., and Hillenbrand, C. D.: Analysing the timing of peak warming
1022 and minimum winter sea-ice extent in the Southern Ocean during MIS 5e, *Quaternary Science Reviews*,
1023 229, 106134, <https://doi.org/10.1016/j.quascirev.2019.106134>, 2020.
- 1024 Chadwick, M., Allen, C. S., Sime, L. C., Crosta, X., and Hillenbrand, C. D.: Reconstructing Antarctic
1025 winter sea-ice extent during Marine Isotope Stage 5e, *Clim. Past*, 18, 129-146,
1026 <https://doi.org/10.5194/cp-18-129-2022>, 2022.
- 1027 Chadwick, M., Jones, J., Lawler, K.-A., Prebble, J., Kohfeld, K. E., and Crosta, X.: Understanding
1028 glacial-interglacial changes in Southern Ocean sea ice, *Past Global Changes Magazine*, 27(2), 86,
1029 <https://doi.org/10.22498/pages.27.2.86>, 2019.
- 1030 Clark, P. U., He, F., Golledge, N. R., Mitrovica, J. X., Dutton, A., Hoffman, J. S., and Dendy, S.: Oceanic
1031 forcing of penultimate deglacial and last interglacial sea-level rise, *Nature*, 577, 660-664,
1032 <https://doi.org/10.1038/s41586-020-1931-7>, 2020.
- 1033 Collins, L. G., Pike, J., Allen, C. S., and Hodgson, D. A.: High-resolution reconstruction of southwest
1034 Atlantic sea-ice and its role in the carbon cycle during marine isotope stages 3 and 2,
1035 *Paleoceanography*, 27, <https://doi.org/10.1029/2011PA002264>, 2012.
- 1036 Collins, L. G., Allen, C. S., Pike, J., Hodgson, D. A., Weckström, K., and Massé, G.: Evaluating highly
1037 branched isoprenoid (HBI) biomarkers as a novel Antarctic sea-ice proxy in deep ocean glacial age
1038 sediments, *Quaternary Science Reviews*, 79, 87-98, <https://doi.org/10.1016/j.quascirev.2013.02.004>,
1039 2013.
- 1040 Coren, F., Ceccone, G., Lodolo, E., Zanolla, C., Zitellini, N., Bonazzi, C., and Centonze, J.: Morphology,
1041 seismic structure and tectonic development of the Powell Basin, Antarctica, *Journal of the Geological*
1042 *Society*, 154, 849-862, <https://doi.org/10.1144/gsjgs.154.5.0849>, 1997.
- 1043 Cortese, G. and Abelmann, A.: Radiolarian-based paleotemperatures during the last 160 kyr at ODP
1044 Site 1089 (Southern Ocean, Atlantic Sector), *Palaeogeography, Palaeoclimatology, Palaeoecology*,
1045 182, 259-286, [https://doi.org/10.1016/S0031-0182\(01\)00499-0](https://doi.org/10.1016/S0031-0182(01)00499-0), 2002.
- 1046 Crosta, X., Denis, D., and Ther, O.: Sea ice seasonality during the Holocene, Adélie Land, East
1047 Antarctica, *Marine Micropaleontology*, 66, 222-232, <https://doi.org/10.1016/j.marmicro.2007.10.001>,
1048 2008.

- 1049 Crosta, X., Pichon, J.-J., and Labracherie, M.: Distribution of Chaetoceros resting spores in modern
1050 peri-Antarctic sediments, *Marine Micropaleontology*, 29, 283-299, [https://doi.org/10.1016/S0377-](https://doi.org/10.1016/S0377-8398(96)00033-3)
1051 [8398\(96\)00033-3](https://doi.org/10.1016/S0377-8398(96)00033-3), 1997.
- 1052 Crosta, X., Kohfeld, K. E., Bostock, H. C., Chadwick, M., Du Vivier, A., Esper, O., Etourneau, J., Jones,
1053 J., Leventer, A., Müller, J., Rhodes, R. H., Allen, C. S., Ghadi, P., Lamping, N., Lange, C. B., Lawler, K.
1054 A., Lund, D., Marzocchi, A., Meissner, K. J., Menviel, L., Nair, A., Patterson, M., Pike, J., Prebble, J. G.,
1055 Riesselman, C., Sadatzki, H., Sime, L. C., Shukla, S. K., Thöle, L., Vorrath, M. E., Xiao, W., and Yang,
1056 J.: Antarctic sea ice over the past 130,000 years – Part 1: a review of what proxy records tell us, *Clim.*
1057 *Past*, 18, 1729-1756, <https://doi.org/10.5194/cp-18-1729-2022>, 2022.
- 1058 Dallmeyer, A., Claussen, M., Wang, Y., and Herzschuh, U.: Spatial variability of Holocene changes in
1059 the annual precipitation pattern: a model-data synthesis for the Asian monsoon region, *Climate*
1060 *Dynamics*, 40, 2919-2936, <https://doi.org/10.1007/s00382-012-1550-6>, 2013.
- 1061 Dallmeyer, A., Claussen, M., Fischer, N., Haberkorn, K., Wagner, S., Pfeiffer, M., Jin, L., Khon, V.,
1062 Wang, Y., and Herzschuh, U.: The evolution of sub-monsoon systems in the Afro-Asian monsoon region
1063 during the Holocene—comparison of different transient climate model simulations, *Clim. Past*,
1064 11, 305-326, <https://doi.org/10.5194/cp-11-305-2015>, 2015.
- 1065 Davies, B. J., Hambrey, M. J., Smellie, J. L., Carrivick, J. L., and Glasser, N. F.: Antarctic Peninsula Ice
1066 Sheet evolution during the Cenozoic Era, *Quaternary Science Reviews*, 31, 30-66,
1067 <https://doi.org/10.1016/j.quascirev.2011.10.012>, 2012.
- 1068 de Vernal, A., Gersonde, R., Goosse, H., Seidenkrantz, M.-S., and Wolff, E. W.: Sea ice in the
1069 paleoclimate system: the challenge of reconstructing sea ice from proxies – an introduction, *Quaternary*
1070 *Science Reviews*, 79, 1-8, <https://doi.org/10.1016/j.quascirev.2013.08.009>, 2013.
- 1071 Deacon, G.: The hydrography of the southern ocean, *Discovery Rep*, 15, 1-124, 1937.
- 1072 DeConto, R. M. and Pollard, D.: Contribution of Antarctica to past and future sea-level rise, *Nature*, 531,
1073 591-597, <https://doi.org/10.1038/nature17145>, 2016.
- 1074 Denis, D., Crosta, X., Barbara, L., Massé, G., Renssen, H., Ther, O., and Giraudeau, J.: Sea ice and
1075 wind variability during the Holocene in East Antarctica: insight on middle–high latitude coupling,
1076 *Quaternary Science Reviews*, 29, 3709-3719, <https://doi.org/10.1016/j.quascirev.2010.08.007>, 2010.
- 1077 Denton, G. H., Anderson, R. F., Toggweiler, J. R., Edwards, R. L., Schaefer, J. M., and Putnam, A. E.:
1078 The Last Glacial Termination, *Science*, 328, 1652-1656, <https://doi.org/10.1126/science.1184119>,
1079 2010.
- 1080 Dickens, W. A., Graham, A. G. C., Smith, J. A., Dowdeswell, J. A., Larter, R. D., Hillenbrand, C.-D.,
1081 Trathan, P. N., Erik Arndt, J., and Kuhn, G.: A new bathymetric compilation for the South Orkney Islands
1082 region, Antarctic Peninsula (49°–39°W to 64°–59°S): Insights into the glacial development of the
1083 continental shelf, *Geochemistry, Geophysics, Geosystems*, 15, 2494-2514,
1084 <https://doi.org/10.1002/2014GC005323>, 2014.
- 1085 Dieckmann, G. S. and Hellmer, H. H.: The importance of sea ice: an overview, in: *Sea ice*, edited by:
1086 Dieckmann, G. S., and Hellmer, H. H., Blackwell Science Ltd, 1-22, 2010.
- 1087 Dorschel, B.: The Expedition PS118 of the Research Vessel POLARSTERN to the Weddell Sea in
1088 2019, Alfred Wegener Institute for Polar and Marine Research, Bremerhaven,
1089 https://doi.org/10.2312/BzPM_0735_2019, 2019.
- 1090 Ebert, E. E., Schramm, J. L., and Curry, J. A.: Disposition of solar radiation in sea ice and the upper
1091 ocean, *Journal of Geophysical Research: Oceans*, 100, 15965-15975,
1092 <https://doi.org/10.1029/95JC01672>, 1995.

- 1093 Elling, F. J., Könneke, M., Mußmann, M., Greve, A., and Hinrichs, K.-U.: Influence of temperature, pH,
 1094 and salinity on membrane lipid composition and TEX86 of marine planktonic thaumarchaeal isolates,
 1095 *Geochimica et Cosmochimica Acta*, 171, 238-255, <https://doi.org/10.1016/j.gca.2015.09.004>, 2015.
- 1096 Elling, F. J., Könneke, M., Lipp, J. S., Becker, K. W., Gagen, E. J., and Hinrichs, K.-U.: Effects of growth
 1097 phase on the membrane lipid composition of the thaumarchaeon *Nitrosopumilus maritimus* and their
 1098 implications for archaeal lipid distributions in the marine environment, *Geochimica et Cosmochimica*
 1099 *Acta*, 141, 579-597, <https://doi.org/10.1016/j.gca.2014.07.005>, 2014.
- 1100 EPICA Community Members: One-to-one coupling of glacial climate variability in Greenland and
 1101 Antarctica, *Nature*, 444, 195-198, <https://doi.org/10.1038/nature05301>, 2006.
- 1102 Esper, O. and Gersonde, R.: New tools for the reconstruction of Pleistocene Antarctic sea ice,
 1103 *Palaeogeography, Palaeoclimatology, Palaeoecology*, 399, 260-283,
 1104 <https://doi.org/10.1016/j.palaeo.2014.01.019>, 2014a.
- 1105 Esper, O. and Gersonde, R.: Quaternary surface water temperature estimations: New diatom transfer
 1106 functions for the Southern Ocean, *Palaeogeography, Palaeoclimatology, Palaeoecology*, 414, 1-19,
 1107 <https://doi.org/10.1016/j.palaeo.2014.08.008>, 2014b.
- 1108 Etourneau, J., Collins, L. G., Willmott, V., Kim, J. H., Barbara, L., Leventer, A., Schouten, S., Sinninghe
 1109 Damsté, J. S., Bianchini, A., Klein, V., Crosta, X., and Massé, G.: Holocene climate variations in the
 1110 western Antarctic Peninsula: evidence for sea ice extent predominantly controlled by changes in
 1111 insolation and ENSO variability, *Clim. Past*, 9, 1431-1446, <https://doi.org/10.5194/cp-9-1431-2013>,
 1112 2013.
- 1113 Fahrback, E., Rohardt, G., and Krause, G.: The Antarctic coastal current in the southeastern Weddell
 1114 Sea, *Polar Biology*, 12, 171-182, <https://doi.org/10.1007/BF00238257>, 1992.
- 1115 Fedotova, A. A. and Stepanova, S. V.: Water Mass Transformation in the Powell Basin, in: *Antarctic*
 1116 *Peninsula Region of the Southern Ocean: Oceanography and Ecology*, edited by: Morozov, E. G., Flint,
 1117 M. V., and Spiridonov, V. A., Springer International Publishing, Cham, 115-129,
 1118 https://doi.org/10.1007/978-3-030-78927-5_8, 2021.
- 1119 Ferrari, R., Jansen, M. F., Adkins, J. F., Burke, A., Stewart, A. L., and Thompson, A. F.: Antarctic sea
 1120 ice control on ocean circulation in present and glacial climates, *Proceedings of the National Academy*
 1121 *of Sciences*, 111, 8753-8758, <https://doi.org/10.1073/pnas.1323922111>, 2014.
- 1122 Fietz, S., Ho, S. L., and Huguet, C.: Archaeal Membrane Lipid-Based Paleothermometry for
 1123 Applications in Polar Oceans, *Oceanography*, 33, 104-114, <https://www.jstor.org/stable/26937748>,
 1124 2020.
- 1125 Fischer, H., Fundel, F., Ruth, U., Twarloh, B., Wegner, A., Udisti, R., Becagli, S., Castellano, E.,
 1126 Morganti, A., Severi, M., Wolff, E., Littot, G., Röthlisberger, R., Mulvaney, R., Hutterli, M. A., Kaufmann,
 1127 P., Federer, U., Lambert, F., Bigler, M., Hansson, M., Jonsell, U., de Angelis, M., Boutron, C., Siggaard-
 1128 Andersen, M.-L., Steffensen, J. P., Barbante, C., Gaspari, V., Gabrielli, P., and Wagenbach, D.:
 1129 Reconstruction of millennial changes in dust emission, transport and regional sea ice coverage using
 1130 the deep EPICA ice cores from the Atlantic and Indian Ocean sector of Antarctica, *Earth and Planetary*
 1131 *Science Letters*, 260, 340-354, <https://doi.org/10.1016/j.epsl.2007.06.014>, 2007.
- 1132 Geibert, W., Stimac, I., Rutgers Van Der Loeff, M., and Kuhn, G.: Dating Deep-Sea Sediments With
 1133 ²³⁰Th Excess Using a Constant Rate of Supply Model, *Paleoceanography and Paleoclimatology*, 34,
 1134 1895-1912, <https://doi.org/10.1029/2019PA003663>, 2019.
- 1135 Gersonde, R. and Zielinski, U.: The reconstruction of late Quaternary Antarctic sea-ice distribution—
 1136 the use of diatoms as a proxy for sea-ice, *Palaeogeography, Palaeoclimatology, Palaeoecology*, 162,
 1137 263-286, [https://doi.org/10.1016/S0031-0182\(00\)00131-0](https://doi.org/10.1016/S0031-0182(00)00131-0), 2000.
- 1138 Gersonde, R., Crosta, X., Abelmann, A., and Armand, L.: Sea-surface temperature and sea ice
 1139 distribution of the Southern Ocean at the EPILOG Last Glacial Maximum—a circum-Antarctic view

- 1140 based on siliceous microfossil records, *Quaternary Science Reviews*, 24, 869-896,
1141 <https://doi.org/10.1016/j.quascirev.2004.07.015>, 2005.
- 1142 Gersonde, R., Abelmann, A., Brathauer, U., Becquey, S., Bianchi, C., Cortese, G., Grobe, H., Kuhn, G.,
1143 Niebler, H.-S., Segl, M., Sieger, R., Zielinski, U., and Fütterer, D. K.: Last glacial sea surface
1144 temperatures and sea-ice extent in the Southern Ocean (Atlantic-Indian sector): A multiproxy approach,
1145 *Paleoceanography*, 18, <https://doi.org/10.1029/2002PA000809>, 2003.
- 1146 Goelzer, H., Huybrechts, P., Loutre, M. F., and Fichet, T.: Last Interglacial climate and sea-level
1147 evolution from a coupled ice sheet–climate model, *Clim. Past*, 12, 2195-2213,
1148 <https://doi.org/10.5194/cp-12-2195-2016>, 2016.
- 1149 Gordon, A. L., Visbeck, M., and Huber, B.: Export of Weddell Sea deep and bottom water, *Journal of*
1150 *Geophysical Research: Oceans*, 106, 9005-9017, <https://doi.org/10.1029/2000JC000281>, 2001.
- 1151 Greene, C. A., Young, D. A., Gwyther, D. E., Galton-Fenzi, B. K., and Blankenship, D. D.: Seasonal
1152 dynamics of Totten Ice Shelf controlled by sea ice buttressing, *The Cryosphere*, 12, 2869-2882,
1153 <https://doi.org/10.5194/tc-12-2869-2018>, 2018.
- 1154 Guagnin, M., Jennings, R., Eager, H., Parton, A., Stimpson, C., Stepanek, C., Pfeiffer, M., Groucutt, H.
1155 S., Drake, N. A., Alsharekh, A., and Petraglia, M. D.: Rock art imagery as a proxy for Holocene
1156 environmental change: A view from Shuwaymis, NW Saudi Arabia, *The Holocene*, 26, 1822-1834,
1157 <https://doi.org/10.1177/0959683616645949>, 2016.
- 1158 Hagemann, J. R., Lembke-Jene, L., Lamy, F., Vorrath, M. E., Kaiser, J., Müller, J., Arz, H. W., Hefter,
1159 J., Jaeschke, A., Ruggieri, N., and Tiedemann, R.: Upper-ocean temperature characteristics in the
1160 subantarctic southeastern Pacific based on biomarker reconstructions, *Clim. Past*, 19, 1825-1845,
1161 <https://doi.org/10.5194/cp-19-1825-2023>, 2023.
- 1162 Haywood, A. M., Hill, D. J., Dolan, A. M., Otto-Bliesner, B. L., Bragg, F., Chan, W. L., Chandler, M. A.,
1163 Contoux, C., Dowsett, H. J., Jost, A., Kamae, Y., Lohmann, G., Lunt, D. J., Abe-Ouchi, A., Pickering,
1164 S. J., Ramstein, G., Rosenbloom, N. A., Salzmann, U., Sohl, L., Stepanek, C., Ueda, H., Yan, Q., and
1165 Zhang, Z.: Large-scale features of Pliocene climate: results from the Pliocene Model Intercomparison
1166 Project, *Clim. Past*, 9, 191-209, <https://doi.org/10.5194/cp-9-191-2013>, 2013.
- 1167 Heroy, D. C., Sjunneskog, C., and Anderson, J. B.: Holocene climate change in the Bransfield Basin,
1168 Antarctic Peninsula: evidence from sediment and diatom analysis, *Antarctic Science*, 20, 69-87,
1169 <https://doi.org/10.1017/S0954102007000788>, 2008.
- 1170 Herron, M. J. and Anderson, J. B.: Late quaternary glacial history of the South Orkney Plateau,
1171 Antarctica, *Quaternary Research*, 33, 265-275, [https://doi.org/10.1016/0033-5894\(90\)90055-P](https://doi.org/10.1016/0033-5894(90)90055-P), 1990.
- 1172 Hibler, W. D.: A Dynamic Thermodynamic Sea Ice Model, *Journal of Physical Oceanography*, 9, 815-
1173 846, [https://doi.org/10.1175/1520-0485\(1979\)009<0815:ADTSIM>2.0.CO;2](https://doi.org/10.1175/1520-0485(1979)009<0815:ADTSIM>2.0.CO;2), 1979.
- 1174 Hoffman, J. S., Clark, P. U., Parnell, A. C., and He, F.: Regional and global sea-surface temperatures
1175 during the last interglaciation, *Science*, 355, 276-279, <https://doi.org/10.1126/science.aai8464>, 2017.
- 1176 Holloway, M. D., Sime, L. C., Singarayer, J. S., Tindall, J. C., Bunch, P., and Valdes, P. J.: Antarctic
1177 last interglacial isotope peak in response to sea ice retreat not ice-sheet collapse, *Nature*
1178 *Communications*, 7, 12293, <https://doi.org/10.1038/ncomms12293>, 2016.
- 1179 Holloway, M. D., Sime, L. C., Allen, C. S., Hillenbrand, C. D., Bunch, P., Wolff, E., and Valdes, P. J.:
1180 The spatial structure of the 128 ka Antarctic sea ice minimum, *Geophysical Research Letters*, 44,
1181 11,129-111,139, <https://doi.org/10.1002/2017GL074594>, 2017.
- 1182 Hopmans, E. C., Weijers, J. W. H., Schefuß, E., Herfort, L., Sinninghe Damsté, J. S., and Schouten, S.:
1183 A novel proxy for terrestrial organic matter in sediments based on branched and isoprenoid tetraether
1184 lipids, *Earth and Planetary Science Letters*, 224, 107-116, <https://doi.org/10.1016/j.epsl.2004.05.012>,
1185 2004.

- 1186 Huhn, O., Hellmer, H. H., Rhein, M., Rodehacke, C., Roether, W., Schodlok, M. P., and Schröder, M.:
 1187 Evidence of deep- and bottom-water formation in the western Weddell Sea, Deep Sea Research Part
 1188 II: Topical Studies in Oceanography, 55, 1098-1116, <https://doi.org/10.1016/j.dsr2.2007.12.015>, 2008.
- 1189 Inglis, G. N., Farnsworth, A., Lunt, D., Foster, G. L., Hollis, C. J., Pagani, M., Jardine, P. E., Pearson,
 1190 P. N., Markwick, P., Galsworthy, A. M. J., Raynham, L., Taylor, K. W. R., and Pancost, R. D.: Descent
 1191 toward the Icehouse: Eocene sea surface cooling inferred from GDGT distributions, Paleoceanography,
 1192 30, 1000-1020, <https://doi.org/10.1002/2014PA002723>, 2015.
- 1193 Jacobs, S. S.: On the nature and significance of the Antarctic Slope Front, Marine Chemistry, 35, 9-24,
 1194 [https://doi.org/10.1016/S0304-4203\(09\)90005-6](https://doi.org/10.1016/S0304-4203(09)90005-6), 1991.
- 1195 Jennings, R. P., Singarayer, J., Stone, E. J., Krebs-Kanzow, U., Khon, V., Nisancioglu, K. H., Pfeiffer,
 1196 M., Zhang, X., Parker, A., Parton, A., Groucutt, H. S., White, T. S., Drake, N. A., and Petraglia, M. D.:
 1197 The greening of Arabia: Multiple opportunities for human occupation of the Arabian Peninsula during
 1198 the Late Pleistocene inferred from an ensemble of climate model simulations, Quaternary International,
 1199 382, 181-199, <https://doi.org/10.1016/j.quaint.2015.01.006>, 2015.
- 1200 Johnson, R. G. and Andrews, J. T.: Glacial terminations in the oxygen isotope record of deep sea cores:
 1201 hypothesis of massive Antarctic ice-shelf destruction, Palaeogeography, Palaeoclimatology,
 1202 Palaeoecology, 53, 107-138, [https://doi.org/10.1016/0031-0182\(86\)90041-6](https://doi.org/10.1016/0031-0182(86)90041-6), 1986.
- 1203 Jungclaus, J. H., Keenlyside, N., Botzet, M., Haak, H., Luo, J.-J., Latif, M., Marotzke, J., Mikolajewicz,
 1204 U., and Roeckner, E.: Ocean Circulation and Tropical Variability in the Coupled Model ECHAM5/MPI-
 1205 OM, Journal of Climate, 19, 3952-3972, <https://doi.org/10.1175/JCLI3827.1>, 2006.
- 1206 Kim, J.-H., Crosta, X., Willmott, V., Renssen, H., Bonnin, J., Helmke, P., Schouten, S., and Sinninghe
 1207 Damsté, J. S.: Holocene subsurface temperature variability in the eastern Antarctic continental margin,
 1208 Geophysical Research Letters, 39, <https://doi.org/10.1029/2012GL051157>, 2012.
- 1209 Kim, J.-H., van der Meer, J., Schouten, S., Helmke, P., Willmott, V., Sangiorgi, F., Koç, N., Hopmans,
 1210 E. C., and Damsté, J. S. S.: New indices and calibrations derived from the distribution of crenarchaeal
 1211 isoprenoid tetraether lipids: Implications for past sea surface temperature reconstructions, Geochimica
 1212 et Cosmochimica Acta, 74, 4639-4654, <https://doi.org/10.1016/j.gca.2010.05.027>, 2010.
- 1213 Klein, K., Weniger, G.-C., Ludwig, P., Stepanek, C., Zhang, X., Wegener, C., and Shao, Y.: Assessing
 1214 climatic impact on transition from Neanderthal to anatomically modern human population on Iberian
 1215 Peninsula: a macroscopic perspective, Science Bulletin, 68, 1176-1186,
 1216 <https://doi.org/10.1016/j.scib.2023.04.025>, 2023.
- 1217 Lambeck, K., Purcell, A., Zhao, J., and Svensson, N.-O.: The Scandinavian Ice Sheet: from MIS 4 to
 1218 the end of the Last Glacial Maximum, Boreas, 39, 410-435, <https://doi.org/10.1111/j.1502-3885.2010.00140.x>, 2010.
- 1220 Lamping, N., Müller, J., Esper, O., Hillenbrand, C.-D., Smith, J. A., and Kuhn, G.: Highly branched
 1221 isoprenoids reveal onset of deglaciation followed by dynamic sea-ice conditions in the western
 1222 Amundsen Sea, Antarctica, Quaternary Science Reviews, 228, 106103,
 1223 <https://doi.org/10.1016/j.quascirev.2019.106103>, 2020.
- 1224 Lamping, N., Müller, J., Hefter, J., Mollenhauer, G., Haas, C., Shi, X., Vorrath, M. E., Lohmann, G., and
 1225 Hillenbrand, C. D.: Evaluation of lipid biomarkers as proxies for sea ice and ocean temperatures along
 1226 the Antarctic continental margin, Clim. Past, 17, 2305-2326, <https://doi.org/10.5194/cp-17-2305-2021>,
 1227 2021.
- 1228 Laskar, J., Robutel, P., Joutel, F., Gastineau, M., Correia, A. C. M., and Levrard, B.: A long-term
 1229 numerical solution for the insolation quantities of the Earth, A&A, 428, 261-285,
 1230 <https://doi.org/10.1051/0004-6361:20041335>, 2004.

- 1231 Lee, J. I., Bak, Y.-S., Yoo, K.-C., Lim, H. S., Yoon, H. I., and Yoon, S. H.: Climate changes in the South
1232 Orkney Plateau during the last 8600 years, *The Holocene*, 20, 395-404,
1233 <https://doi.org/10.1177/0959683609353430>, 2010.
- 1234 Leventer, A.: The fate of Antarctic “sea ice diatoms” and their use as paleoenvironmental indicators,
1235 *Antarctic sea ice: biological processes, interactions and variability*, 73, 121-137, 1998.
- 1236 Liu, R., Han, Z., Zhao, J., Zhang, H., Li, D., Ren, J., Pan, J., and Zhang, H.: Distribution and source of
1237 glycerol dialkyl glycerol tetraethers (GDGTs) and the applicability of GDGT-based temperature proxies
1238 in surface sediments of Prydz Bay, East Antarctica, *Polar Research*, 39,
1239 <https://doi.org/10.33265/polar.v39.3557>, 2020.
- 1240 Liu, X.-L., Summons, R. E., and Hinrichs, K.-U.: Extending the known range of glycerol ether lipids in
1241 the environment: structural assignments based on tandem mass spectral fragmentation patterns, *Rapid*
1242 *Communications in Mass Spectrometry*, 26, 2295-2302, <https://doi.org/10.1002/rcm.6355>, 2012a.
- 1243 Liu, X.-L., Lipp, J. S., Simpson, J. H., Lin, Y.-S., Summons, R. E., and Hinrichs, K.-U.: Mono- and
1244 dihydroxyl glycerol dibiphytanyl glycerol tetraethers in marine sediments: Identification of both core and
1245 intact polar lipid forms, *Geochimica et Cosmochimica Acta*, 89, 102-115,
1246 <https://doi.org/10.1016/j.gca.2012.04.053>, 2012b.
- 1247 Locarnini, R. A., Mishonov, A. V., Baranova, O. K., Boyer, T. P., Zweng, M. M., Garcia, H. E., Reagan,
1248 J. R., Seidov, D., Weathers, K., Paver, C. R., and Smolyar, I.: *World Ocean Atlas 2018, Volume 1:*
1249 *Temperature [dataset]*, 2018.
- 1250 Loveland, T. R., Reed, B. C., Brown, J. F., Ohlen, D. O., Zhu, Z., Yang, L., and Merchant, J. W.:
1251 Development of a global land cover characteristics database and IGBP DISCover from 1 km AVHRR
1252 data, *International Journal of Remote Sensing*, 21, 1303-1330,
1253 <https://doi.org/10.1080/014311600210191>, 2000.
- 1254 Lü, X., Liu, X.-L., Elling, F. J., Yang, H., Xie, S., Song, J., Li, X., Yuan, H., Li, N., and Hinrichs, K.-U.:
1255 Hydroxylated isoprenoid GDGTs in Chinese coastal seas and their potential as a paleotemperature
1256 proxy for mid-to-low latitude marginal seas, *Organic Geochemistry*, 89-90, 31-43,
1257 <https://doi.org/10.1016/j.orggeochem.2015.10.004>, 2015.
- 1258 Lunt, D. J., Abe-Ouchi, A., Bakker, P., Berger, A., Braconnot, P., Charbit, S., Fischer, N., Herold, N.,
1259 Jungclauss, J. H., Khon, V. C., Krebs-Kanzow, U., Langebroek, P. M., Lohmann, G., Nisancioglu, K. H.,
1260 Otto-Bliesner, B. L., Park, W., Pfeiffer, M., Phipps, S. J., Prange, M., Rachmayani, R., Renssen, H.,
1261 Rosenbloom, N., Schneider, B., Stone, E. J., Takahashi, K., Wei, W., Yin, Q., and Zhang, Z. S.: A multi-
1262 model assessment of last interglacial temperatures, *Clim. Past*, 9, 699-717, [https://doi.org/10.5194/cp-](https://doi.org/10.5194/cp-9-699-2013)
1263 [9-699-2013](https://doi.org/10.5194/cp-9-699-2013), 2013.
- 1264 Luo, F., Ying, J., Liu, T., and Chen, D.: Origins of Southern Ocean warm sea surface temperature bias
1265 in CMIP6 models, *npj Climate and Atmospheric Science*, 6, 127, [https://doi.org/10.1038/s41612-023-](https://doi.org/10.1038/s41612-023-00456-6)
1266 [00456-6](https://doi.org/10.1038/s41612-023-00456-6), 2023.
- 1267 Marino, G., Rohling, E. J., Rodríguez-Sanz, L., Grant, K. M., Heslop, D., Roberts, A. P., Stanford, J. D.,
1268 and Yu, J.: Bipolar seesaw control on last interglacial sea level, *Nature*, 522, 197-201,
1269 <https://doi.org/10.1038/nature14499>, 2015.
- 1270 Marsland, S. J., Haak, H., Jungclauss, J. H., Latif, M., and Röske, F.: The Max-Planck-Institute global
1271 ocean/sea ice model with orthogonal curvilinear coordinates, *Ocean Modelling*, 5, 91-127,
1272 [https://doi.org/10.1016/S1463-5003\(02\)00015-X](https://doi.org/10.1016/S1463-5003(02)00015-X), 2003.
- 1273 Massé, G., Belt, S. T., Crosta, X., Schmidt, S., Snape, I., Thomas, D. N., and Rowland, S. J.: Highly
1274 branched isoprenoids as proxies for variable sea ice conditions in the Southern Ocean, *Antarctic*
1275 *Science*, 23, 487-498, <https://doi.org/10.1017/S0954102011000381>, 2011.

- 1276 Massom, R. A., Scambos, T. A., Bennetts, L. G., Reid, P., Squire, V. A., and Stammerjohn, S. E.:
 1277 Antarctic ice shelf disintegration triggered by sea ice loss and ocean swell, *Nature*, 558, 383-389,
 1278 <https://doi.org/10.1038/s41586-018-0212-1>, 2018.
- 1279 Massom, R. A., Giles, A. B., Warner, R. C., Fricker, H. A., Legrésy, B., Hyland, G., Lescarmontier, L.,
 1280 and Young, N.: External influences on the Mertz Glacier Tongue (East Antarctica) in the decade leading
 1281 up to its calving in 2010, *Journal of Geophysical Research: Earth Surface*, 120, 490-506,
 1282 <https://doi.org/10.1002/2014JF003223>, 2015.
- 1283 Masson-Delmotte, V., Buiron, D., Ekaykin, A., Frezzotti, M., Gallée, H., Jouzel, J., Krinner, G., Landais,
 1284 A., Motoyama, H., Oerter, H., Pol, K., Pollard, D., Ritz, C., Schlosser, E., Sime, L. C., Sodemann, H.,
 1285 Stenni, B., Uemura, R., and Vimeux, F.: A comparison of the present and last interglacial periods in six
 1286 Antarctic ice cores, *Clim. Past*, 7, 397-423, <https://doi.org/10.5194/cp-7-397-2011>, 2011.
- 1287 Morozov, E. G., Frey, D. I., and Tarakanov, R. Y.: Antarctic Bottom Water Flow through the Eastern
 1288 Part of the Philip Passage in the Weddell Sea, *Oceanology*, 60, 589-592,
 1289 <https://doi.org/10.1134/S000143702005015X>, 2020.
- 1290 Müller, J., Wagner, A., Fahl, K., Stein, R., Prange, M., and Lohmann, G.: Towards quantitative sea ice
 1291 reconstructions in the northern North Atlantic: A combined biomarker and numerical modelling
 1292 approach, *Earth and Planetary Science Letters*, 306, 137-148,
 1293 <https://doi.org/10.1016/j.epsl.2011.04.011>, 2011.
- 1294 Müller, P. J. and Schneider, R.: An automated leaching method for the determination of opal in
 1295 sediments and particulate matter, *Deep Sea Research Part I: Oceanographic Research Papers*, 40,
 1296 425-444, 1993.
- 1297 Naughten, K. A., Meissner, K. J., Galton-Fenzi, B. K., England, M. H., Timmermann, R., Hellmer, H. H.,
 1298 Hattermann, T., and Debernard, J. B.: Intercomparison of Antarctic ice-shelf, ocean, and sea-ice
 1299 interactions simulated by MetROMS-iceshelf and FESOM 1.4, *Geosci. Model Dev.*, 11, 1257-1292,
 1300 <https://doi.org/10.5194/gmd-11-1257-2018>, 2018.
- 1301 Naveira Garabato, A. C., McDonagh, E. L., Stevens, D. P., Heywood, K. J., and Sanders, R. J.: On the
 1302 export of Antarctic Bottom Water from the Weddell Sea, *Deep Sea Research Part II: Topical Studies in*
 1303 *Oceanography*, 49, 4715-4742, [https://doi.org/10.1016/S0967-0645\(02\)00156-X](https://doi.org/10.1016/S0967-0645(02)00156-X), 2002.
- 1304 Ó Cofaigh, C., Davies, B. J., Livingstone, S. J., Smith, J. A., Johnson, J. S., Hocking, E. P., Hodgson,
 1305 D. A., Anderson, J. B., Bentley, M. J., Canals, M., Domack, E., Dowdeswell, J. A., Evans, J., Glasser,
 1306 N. F., Hillenbrand, C.-D., Larter, R. D., Roberts, S. J., and Simms, A. R.: Reconstruction of ice-sheet
 1307 changes in the Antarctic Peninsula since the Last Glacial Maximum, *Quaternary Science Reviews*, 100,
 1308 87-110, <https://doi.org/10.1016/j.quascirev.2014.06.023>, 2014.
- 1309 Olbers, D., Gouretsky, V., Seiss, G., and Schröter, J.: Hydrographic atlas of the Southern Ocean, Alfred-
 1310 Wegener-Institut, Bremerhaven 1992.
- 1311 Orsi, A. H., Johnson, G. C., and Bullister, J. L.: Circulation, mixing, and production of Antarctic Bottom
 1312 Water, *Progress in Oceanography*, 43, 55-109, [https://doi.org/10.1016/S0079-6611\(99\)00004-X](https://doi.org/10.1016/S0079-6611(99)00004-X), 1999.
- 1313 Orsi, A. H., Nowlin, W. D., and Whitworth, T.: On the circulation and stratification of the Weddell Gyre,
 1314 *Deep Sea Research Part I: Oceanographic Research Papers*, 40, 169-203,
 1315 [https://doi.org/10.1016/0967-0637\(93\)90060-G](https://doi.org/10.1016/0967-0637(93)90060-G), 1993.
- 1316 Orsi, A. H., Whitworth, T., and Nowlin, W. D.: On the meridional extent and fronts of the Antarctic
 1317 Circumpolar Current, *Deep Sea Research Part I: Oceanographic Research Papers*, 42, 641-673,
 1318 [https://doi.org/10.1016/0967-0637\(95\)00021-W](https://doi.org/10.1016/0967-0637(95)00021-W), 1995.
- 1319 Otto-Bliesner, B. L., Rosenbloom, N., Stone, E. J., McKay, N. P., Lunt, D. J., Brady, E. C., and
 1320 Overpeck, J. T.: How warm was the last interglacial? New model–data comparisons, *Philosophical*
 1321 *Transactions of the Royal Society A: Mathematical, Physical and Engineering Sciences*, 371,
 1322 20130097, <https://doi.org/10.1098/rsta.2013.0097>, 2013.

- 1323 Otto-Bliesner, B. L., Braconnot, P., Harrison, S. P., Lunt, D. J., Abe-Ouchi, A., Albani, S., Bartlein, P.
 1324 J., Capron, E., Carlson, A. E., Dutton, A., Fischer, H., Goelzer, H., Govin, A., Haywood, A., Joos, F.,
 1325 LeGrande, A. N., Lipscomb, W. H., Lohmann, G., Mahowald, N., Nehrbass-Ahles, C., Pausata, F. S.
 1326 R., Peterschmitt, J. Y., Phipps, S. J., Renssen, H., and Zhang, Q.: The PMIP4 contribution to CMIP6 –
 1327 Part 2: Two interglacials, scientific objective and experimental design for Holocene and Last Interglacial
 1328 simulations, *Geosci. Model Dev.*, 10, 3979-4003, <https://doi.org/10.5194/gmd-10-3979-2017>, 2017.
- 1329 Park, E., Heffer, J., Fischer, G., Iversen, M. H., Ramondenc, S., Nöthig, E. M., and Mollenhauer, G.:
 1330 Seasonality of archaeal lipid flux and GDGT-based thermometry in sinking particles of high-latitude
 1331 oceans: Fram Strait (79°N) and Antarctic Polar Front (50°S), *Biogeosciences*, 16, 2247-2268,
 1332 <https://doi.org/10.5194/bg-16-2247-2019>, 2019.
- 1333 Pedro, J. B., van Ommen, T. D., Rasmussen, S. O., Morgan, V. I., Chappellaz, J., Moy, A. D., Masson-
 1334 Delmotte, V., and Delmotte, M.: The last deglaciation: timing the bipolar seesaw, *Clim. Past*, 7, 671-
 1335 683, <https://doi.org/10.5194/cp-7-671-2011>, 2011.
- 1336 Pedro, J. B., Bostock, H. C., Bitz, C. M., He, F., Vandergoes, M. J., Steig, E. J., Chase, B. M., Krause,
 1337 C. E., Rasmussen, S. O., Markle, B. R., and Cortese, G.: The spatial extent and dynamics of the
 1338 Antarctic Cold Reversal, *Nature Geoscience*, 9, 51-55, <https://doi.org/10.1038/ngeo2580>, 2016.
- 1339 Pellichero, V., Sallée, J.-B., Chapman, C. C., and Downes, S. M.: The southern ocean meridional
 1340 overturning in the sea-ice sector is driven by freshwater fluxes, *Nature Communications*, 9, 1789,
 1341 <https://doi.org/10.1038/s41467-018-04101-2>, 2018.
- 1342 Pfeiffer, M. and Lohmann, G.: Greenland Ice Sheet influence on Last Interglacial climate: global
 1343 sensitivity studies performed with an atmosphere–ocean general circulation model, *Clim. Past*, 12,
 1344 1313-1338, <https://doi.org/10.5194/cp-12-1313-2016>, 2016.
- 1345 Pitcher, A., Hopmans, E. C., Mosier, A. C., Park, S. J., Rhee, S. K., Francis, C. A., Schouten, S., and
 1346 Sinninghe Damsté, J. S.: Core and intact polar glycerol dibiphytanyl glycerol tetraether lipids of
 1347 ammonia-oxidizing Archaea enriched from marine and estuarine sediments, *Applied and Environmental*
 1348 *Microbiology*, 77, 3468-3477, <https://doi.org/10.1128/AEM.02758-10>, 2011.
- 1349 Pollard, D. and DeConto, R. M.: Modelling West Antarctic ice sheet growth and collapse through the
 1350 past five million years, *Nature*, 458, 329-332, <https://doi.org/10.1038/nature07809>, 2009.
- 1351 Raddatz, T. J., Reick, C. H., Knorr, W., Kattge, J., Roeckner, E., Schnur, R., Schnitzler, K. G., Wetzel,
 1352 P., and Jungclaus, J.: Will the tropical land biosphere dominate the climate–carbon cycle feedback
 1353 during the twenty-first century?, *Climate Dynamics*, 29, 565-574, [https://doi.org/10.1007/s00382-007-](https://doi.org/10.1007/s00382-007-0247-8)
 1354 [0247-8](https://doi.org/10.1007/s00382-007-0247-8), 2007.
- 1355 Reynolds, R. W., Rayner, N. A., Smith, T. M., Stokes, D. C., and Wang, W.: An Improved In Situ and
 1356 Satellite SST Analysis for Climate, *Journal of Climate*, 15, 1609-1625, [https://doi.org/10.1175/1520-](https://doi.org/10.1175/1520-0442(2002)015<1609:AIISAS>2.0.CO;2)
 1357 [0442\(2002\)015<1609:AIISAS>2.0.CO;2](https://doi.org/10.1175/1520-0442(2002)015<1609:AIISAS>2.0.CO;2), 2002.
- 1358 Reynolds, R. W., Smith, T. M., Liu, C., Chelton, D. B., Casey, K. S., and Schlax, M. G.: Daily High-
 1359 Resolution-Blended Analyses for Sea Surface Temperature, *Journal of Climate*, 20, 5473-5496,
 1360 <https://doi.org/10.1175/2007JCLI1824.1>, 2007.
- 1361 Rhodes, R., Kohfeld, K., Bostock, H., Crosta, X., Leventer, A., Meissner, K., and Esper, O.:
 1362 Understanding past changes in sea ice in the Southern Ocean, *Past Global Changes Magazine*, 27(1),
 1363 31, <https://doi.org/10.22498/pages.27.1.31>, 2019.
- 1364 Riaux-Gobin, C. and Poulin, M.: Possible symbiosis of *Berkeleya adeliensis* Medlin, *Synedropsis fragilis*
 1365 (Manguin) Hasle et al. and *Nitzschia lecontei* Van Heurck (Bacillariophyta) associated with land-fast
 1366 ice in Adélie Land, Antarctica, *Diatom Research*, 19, 265-274, 2004.
- 1367 Rintoul, S. R.: The global influence of localized dynamics in the Southern Ocean, *Nature*, 558, 209-218,
 1368 <https://doi.org/10.1038/s41586-018-0182-3>, 2018.

- 1369 Robel, A. A.: Thinning sea ice weakens buttressing force of iceberg mélange and promotes calving,
1370 Nature Communications, 8, 14596, <https://doi.org/10.1038/ncomms14596>, 2017.
- 1371 Rohling, E. J., Hibbert, F. D., Williams, F. H., Grant, K. M., Marino, G., Foster, G. L., Hennekam, R., de
1372 Lange, G. J., Roberts, A. P., Yu, J., Webster, J. M., and Yokoyama, Y.: Differences between the last
1373 two glacial maxima and implications for ice-sheet, $\delta^{18}\text{O}$, and sea-level reconstructions, Quaternary
1374 Science Reviews, 176, 1-28, <https://doi.org/10.1016/j.quascirev.2017.09.009>, 2017.
- 1375 Ryves, D. B., Battarbee, R. W., and Fritz, S. C.: The dilemma of disappearing diatoms: Incorporating
1376 diatom dissolution data into palaeoenvironmental modelling and reconstruction, Quaternary Science
1377 Reviews, 28, 120-136, <https://doi.org/10.1016/j.quascirev.2008.08.021>, 2009.
- 1378 Sadatzki, H., Opdyke, B., Menviel, L., Leventer, A., Hope, J. M., Brocks, J. J., Fallon, S., Post, A. L.,
1379 O'Brien, P. E., Grant, K., and Armand, L.: Early sea ice decline off East Antarctica at the last glacial–
1380 interglacial climate transition, Science Advances, 9, eadh9513, <https://doi.org/10.1126/sciadv.adh9513>,
1381 2023.
- 1382 Seabrooke, J. M., Hufford, G. L., and Elder, R. B.: Formation of Antarctic bottom water in the Weddell
1383 Sea, Journal of Geophysical Research (1896-1977), 76, 2164-2178,
1384 <https://doi.org/10.1029/JC076i009p02164>, 1971.
- 1385 Shevenell, A. E., Domack, E. W., and Kernan, G. M.: Record of Holocene palaeoclimate change along
1386 the Antarctic Peninsula: evidence from glacial marine sediments, Lallemand Fjord, Papers and
1387 Proceedings of the Royal Society of Tasmania, 55-64,
- 1388 Sinninghe Damsté, J. S., Rijpstra, W. I. C., Hopmans, E. C., Jung, J., Kim, J. H., Rhee, S. K.,
1389 Stieglmeier, M., and Schleper, C.: Intact Polar and Core Glycerol Dibiphytanyl Glycerol Tetraether
1390 Lipids of Group I.1a and I.1b Thaumarchaeota in Soil, Applied and Environmental Microbiology, 78,
1391 6866-6874, <https://doi.org/10.1128/AEM.01681-12>, 2012.
- 1392 Smik, L., Belt, S. T., Lieser, J. L., Armand, L. K., and Leventer, A.: Distributions of highly branched
1393 isoprenoid alkenes and other algal lipids in surface waters from East Antarctica: Further insights for
1394 biomarker-based paleo sea-ice reconstruction, Organic Geochemistry, 95, 71-80,
1395 <https://doi.org/10.1016/j.orggeochem.2016.02.011>, 2016.
- 1396 Stepanek, C. and Lohmann, G.: Modelling mid-Pliocene climate with COSMOS, Geosci. Model Dev.,
1397 5, 1221-1243, <https://doi.org/10.5194/gmd-5-1221-2012>, 2012.
- 1398 Stepanek, C., Samakinwa, E., Knorr, G., and Lohmann, G.: Contribution of the coupled atmosphere–
1399 ocean–sea ice–vegetation model COSMOS to the PlioMIP2, Clim. Past, 16, 2275-2323,
1400 <https://doi.org/10.5194/cp-16-2275-2020>, 2020.
- 1401 Stevens, B., Giorgetta, M., Esch, M., Mauritsen, T., Crueger, T., Rast, S., Salzmann, M., Schmidt, H.,
1402 Bader, J., Block, K., Brokopf, R., Fast, I., Kinne, S., Kornblueh, L., Lohmann, U., Pincus, R., Reichler,
1403 T., and Roeckner, E.: Atmospheric component of the MPI-M Earth System Model: ECHAM6, Journal of
1404 Advances in Modeling Earth Systems, 5, 146-172, <https://doi.org/10.1002/jame.20015>, 2013.
- 1405 Sutter, J., Gierz, P., Grosfeld, K., Thoma, M., and Lohmann, G.: Ocean temperature thresholds for Last
1406 Interglacial West Antarctic Ice Sheet collapse, Geophysical Research Letters, 43, 2675-2682,
1407 <https://doi.org/10.1002/2016GL067818>, 2016.
- 1408 Tarasov, L., Dyke, A. S., Neal, R. M., and Peltier, W. R.: A data-calibrated distribution of deglacial
1409 chronologies for the North American ice complex from glaciological modeling, Earth and Planetary
1410 Science Letters, 315-316, 30-40, <https://doi.org/10.1016/j.epsl.2011.09.010>, 2012.
- 1411 Taylor, F. and Sjunneskog, C.: Postglacial marine diatom record of the Palmer Deep, Antarctic
1412 Peninsula (ODP Leg 178, Site 1098) 2. Diatom assemblages, Paleoceanography, 17, PAL 2-1-PAL 2-
1413 12, <https://doi.org/10.1029/2000PA000564>, 2002.

- 1414 Taylor, F., Whitehead, J., and Domack, E.: Holocene paleoclimate change in the Antarctic Peninsula:
 1415 evidence from the diatom, sedimentary and geochemical record, *Marine Micropaleontology*, 41, 25-43,
 1416 [https://doi.org/10.1016/S0377-8398\(00\)00049-9](https://doi.org/10.1016/S0377-8398(00)00049-9), 2001.
- 1417 Thompson, A. F., Stewart, A. L., Spence, P., and Heywood, K. J.: The Antarctic Slope Current in a
 1418 Changing Climate, *Reviews of Geophysics*, 56, 741-770, <https://doi.org/10.1029/2018RG000624>,
 1419 2018.
- 1420 Turney, C. S. M., Fogwill, C. J., Golledge, N. R., McKay, N. P., van Sebille, E., Jones, R. T., Etheridge,
 1421 D., Rubino, M., Thornton, D. P., Davies, S. M., Ramsey, C. B., Thomas, Z. A., Bird, M. I., Munksgaard,
 1422 N. C., Kohno, M., Woodward, J., Winter, K., Weyrich, L. S., Rootes, C. M., Millman, H., Albert, P. G.,
 1423 Rivera, A., van Ommen, T., Curran, M., Moy, A., Rahmstorf, S., Kawamura, K., Hillenbrand, C.-D.,
 1424 Weber, M. E., Manning, C. J., Young, J., and Cooper, A.: Early Last Interglacial ocean warming drove
 1425 substantial ice mass loss from Antarctica, *Proceedings of the National Academy of Sciences*, 117,
 1426 3996-4006, <https://doi.org/10.1073/pnas.1902469117>, 2020.
- 1427 Varma, V., Prange, M., Merkel, U., Kleinen, T., Lohmann, G., Pfeiffer, M., Renssen, H., Wagner, A.,
 1428 Wagner, S., and Schulz, M.: Holocene evolution of the Southern Hemisphere westerly winds in transient
 1429 simulations with global climate models, *Clim. Past*, 8, 391-402, <https://doi.org/10.5194/cp-8-391-2012>,
 1430 2012.
- 1431 Vaughan, D. G., Comiso, J. C., Allison, I., Carrasco, J., Kaser, G., Kwok, R., Mote, P., Murray, T., Paul,
 1432 F., Ren, J., Rigno, E., Solomina, O., Steffen, K., and Zhang, T.: *Observations: Cryosphere*, Cambridge
 1433 University Press, Cambridge, United Kingdom and New York, NY, USA, 2013.
- 1434 Vernet, M., Geibert, W., Hoppema, M., Brown, P. J., Haas, C., Hellmer, H. H., Jokat, W., Jullion, L.,
 1435 Mazloff, M., Bakker, D. C. E., Brearley, J. A., Croot, P., Hattermann, T., Hauck, J., Hillenbrand, C.-D.,
 1436 Hoppe, C. J. M., Huhn, O., Koch, B. P., Lechtenfeld, O. J., Meredith, M. P., Naveira Garabato, A. C.,
 1437 Nöthig, E.-M., Peeken, I., Rutgers van der Loeff, M. M., Schmidtke, S., Schröder, M., Strass, V. H.,
 1438 Torres-Valdés, S., and Verdy, A.: The Weddell Gyre, Southern Ocean: Present Knowledge and Future
 1439 Challenges, *Reviews of Geophysics*, 57, 623-708, <https://doi.org/10.1029/2018RG000604>, 2019.
- 1440 Viseras, C. and Maldonado, A.: Facies architecture, seismic stratigraphy and development of a high-
 1441 latitude basin: the Powell Basin (Antarctica), *Marine Geology*, 157, 69-87,
 1442 [https://doi.org/10.1016/S0025-3227\(98\)00136-4](https://doi.org/10.1016/S0025-3227(98)00136-4), 1999.
- 1443 Vorrath, M. E., Müller, J., Esper, O., Mollenhauer, G., Haas, C., Schefuß, E., and Fahl, K.: Highly
 1444 branched isoprenoids for Southern Ocean sea ice reconstructions: a pilot study from the Western
 1445 Antarctic Peninsula, *Biogeosciences*, 16, 2961-2981, <https://doi.org/10.5194/bg-16-2961-2019>, 2019.
- 1446 Vorrath, M. E., Müller, J., Rebolledo, L., Cárdenas, P., Shi, X., Esper, O., Opel, T., Geibert, W., Muñoz,
 1447 P., Haas, C., Kuhn, G., Lange, C. B., Lohmann, G., and Mollenhauer, G.: Sea ice dynamics in the
 1448 Bransfield Strait, Antarctic Peninsula, during the past 240 years: a multi-proxy intercomparison study,
 1449 *Clim. Past*, 16, 2459-2483, <https://doi.org/10.5194/cp-16-2459-2020>, 2020.
- 1450 Vorrath, M. E., Müller, J., Cárdenas, P., Opel, T., Mieruch, S., Esper, O., Lembke-Jene, L., Etourneau,
 1451 J., Vieth-Hillebrand, A., Lahajnar, N., Lange, C. B., Leventer, A., Evangelinos, D., Escutia, C., and
 1452 Mollenhauer, G.: Deglacial and Holocene sea-ice and climate dynamics in the Bransfield Strait, northern
 1453 Antarctic Peninsula, *Clim. Past*, 19, 1061-1079, <https://doi.org/10.5194/cp-19-1061-2023>, 2023.
- 1454 Waelbroeck, C., Skinner, L. C., Labeyrie, L., Duplessy, J.-C., Michel, E., Vazquez Riveiros, N.,
 1455 Gherardi, J.-M., and Dewilde, F.: The timing of deglacial circulation changes in the Atlantic,
 1456 *Paleoceanography*, 26, <https://doi.org/10.1029/2010PA002007>, 2011.
- 1457 Weber, M. E., Bailey, I., Hemming, S. R., Martos, Y. M., Reilly, B. T., Ronge, T. A., Brachfeld, S.,
 1458 Williams, T., Raymo, M., Belt, S. T., Smik, L., Vogel, H., Peck, V. L., Armbrrecht, L., Cage, A., Cardillo,
 1459 F. G., Du, Z., Fauth, G., Fogwill, C. J., Garcia, M., Garnsworthy, M., Glüder, A., Guitard, M., Gutjahr,
 1460 M., Hernández-Almeida, I., Hoem, F. S., Hwang, J.-H., Iizuka, M., Kato, Y., Kenlee, B., Oconnell, S.,
 1461 Pérez, L. F., Seki, O., Stevens, L., Tauxe, L., Tripathi, S., Warnock, J., and Zheng, X.: Antiphased dust

- 1462 deposition and productivity in the Antarctic Zone over 1.5 million years, *Nature Communications*, 13,
1463 2044, <https://doi.org/10.1038/s41467-022-29642-5>, 2022.
- 1464 Wei, W. and Lohmann, G.: Simulated Atlantic Multidecadal Oscillation during the Holocene, *Journal of*
1465 *Climate*, 25, 6989-7002, <https://doi.org/10.1175/JCLI-D-11-00667.1>, 2012.
- 1466 Williams, T. J., Martin, E. E., Sikes, E., Starr, A., Umling, N. E., and Glaubke, R.: Neodymium isotope
1467 evidence for coupled Southern Ocean circulation and Antarctic climate throughout the last 118,000
1468 years, *Quaternary Science Reviews*, 260, 106915, <https://doi.org/10.1016/j.quascirev.2021.106915>,
1469 2021.
- 1470 Xiao, W., Esper, O., and Gersonde, R.: Last Glacial - Holocene climate variability in the Atlantic sector
1471 of the Southern Ocean, *Quaternary Science Reviews*, 135, 115-137,
1472 <https://doi.org/10.1016/j.quascirev.2016.01.023>, 2016a.
- 1473 Xiao, W., Frederichs, T., Gersonde, R., Kuhn, G., Esper, O., and Zhang, X.: Constraining the dating of
1474 late Quaternary marine sediment records from the Scotia Sea (Southern Ocean), *Quaternary*
1475 *Geochronology*, 31, 97-118, <https://doi.org/10.1016/j.quageo.2015.11.003>, 2016b.
- 1476 Xiao, W., Xu, Y., Zhang, C., Lin, J., Wu, W., Lü, X., Tan, J., Zhang, X., Zheng, F., Song, X., Zhu, Y.,
1477 Yang, Y., Zhang, H., Wenzhöfer, F., Rowden, A. A., and Glud, R. N.: Disentangling Effects of Sea
1478 Surface Temperature and Water Depth on Hydroxylated Isoprenoid GDGTs: Insights From the Hadal
1479 Zone and Global Sediments, *Geophysical Research Letters*, 50, e2023GL103109,
1480 <https://doi.org/10.1029/2023GL103109>, 2023.
- 1481 Zhang, X., Knorr, G., Lohmann, G., and Barker, S.: Abrupt North Atlantic circulation changes in
1482 response to gradual CO₂ forcing in a glacial climate state, *Nature Geoscience*, 10, 518-523,
1483 <https://doi.org/10.1038/ngeo2974>, 2017.
- 1484 Zhang, X., Lohmann, G., Knorr, G., and Xu, X.: Different ocean states and transient characteristics in
1485 Last Glacial Maximum simulations and implications for deglaciation, *Clim. Past*, 9, 2319-2333,
1486 <https://doi.org/10.5194/cp-9-2319-2013>, 2013.
- 1487 Zhang, Y. G., Pagani, M., and Wang, Z.: Ring Index: A new strategy to evaluate the integrity of TEX₈₆
1488 paleothermometry, *Paleoceanography*, 31, 220-232, <https://doi.org/10.1002/2015PA002848>, 2016.
- 1489 Zielinski, U. and Gersonde, R.: Diatom distribution in Southern Ocean surface sediments (Atlantic
1490 sector): Implications for paleoenvironmental reconstructions, *Palaeogeography, Palaeoclimatology,*
1491 *Palaeoecology*, 129, 213-250, [https://doi.org/10.1016/S0031-0182\(96\)00130-7](https://doi.org/10.1016/S0031-0182(96)00130-7), 1997.
1492